Measurement of initial-state–final-state radiation interference in the processes $e^+e^- \to \mu^+\mu^-\gamma$ and $e^+e^- \to \pi^+\pi^-\gamma$

J. P. Lees,[1] V. Poireau,[1] V. Tisserand,[1] E. Grauges,[2] A. Palano,[3a,3b] G. Eigen,[4] B. Stugu,[4] D. N. Brown,[5] L. T. Kerth,[5] Yu. G. Kolomensky,[5] M. J. Lee,[5] G. Lynch,[5] H. Koch,[6] T. Schroeder,[6] C. Hearty,[7] T. S. Mattison,[7] J. A. McKenna,[7] R. Y. So,[7] A. Khan,[8] V. E. Blinov,[9a,9b,9c] A. R. Buzykaev,[9a] V. P. Druzhinin,[9a,9b] V. B. Golubev,[9a,9b] E. A. Kravchenko,[9a,9b] A. P. Onuchin,[9a,9b,9c] S. I. Serednyakov,[9a,9b] Yu. I. Skovpen,[9a,9b] E. P. Solodov,[9a,9b] K. Yu. Todyshev,[9a,9b] A. J. Lankford,[10] B. Dey,[11] J. W. Gary,[11] O. Long,[11] M. Franco Sevilla,[12] T. M. Hong,[12] D. Kovalskyi,[12] J. D. Richman,[12] C. A. West,[12] A. M. Eisner,[13] W. S. Lockman,[13] W. Panduro Vazquez,[13] B. A. Schumm,[13] A. Seiden,[13] D. S. Chao,[14] C. H. Cheng,[14] B. Echenard,[14] K. T. Flood,[14] D. G. Hitlin,[14] J. Kim,[14] T. S. Miyashita,[14] P. Ongmongkolkul,[14] F. C. Porter,[14] M. Röhrken,[14] R. Andreassen,[15] Z. Huard,[15] B. T. Meadows,[15] B. G. Pushpawela,[15] M. D. Sokoloff,[15] L. Sun,[15] W. T. Ford,[16] J. G. Smith,[16] S. R. Wagner,[16] R. Ayad,[17,†] W. H. Toki,[17] B. Spaan,[18] D. Bernard,[19] M. Verderi,[19] S. Playfer,[20] D. Bettoni,[21a] C. Bozzi,[21a] R. Calabrese,[21a,21b] G. Cibinetto,[21a,21b] E. Fioravanti,[21a,21b] I. Garzia,[21a,21b] E. Luppi,[21a,21b] L. Piemontese,[21a] V. Santoro,[21a] A. Calcaterra,[22] R. de Sangro,[22] G. Finocchiaro,[22] S. Martellotti,[22] P. Patteri,[22] I. M. Peruzzi,[22] M. Piccolo,[22] A. Zallo,[22] R. Contri,[23a,23b] M. R. Monge,[23a,23b] S. Passaggio,[23a] C. Patrignani,[23a,23b] B. Bhuyan,[24] V. Prasad,[24] A. Adametz,[25] U. Uwer,[25] H. M. Lacker,[26] U. Mallik,[27] C. Chen,[28] J. Cochran,[28] S. Prell,[28] H. Ahmed,[29] A. V. Gritsan,[30] N. Arnaud,[31] M. Davier,[31] D. Derkach,[31] G. Grosdidier,[31] F. Le Diberder,[31] A. M. Lutz,[31] B. Malaescu,[31,‡] P. Roudeau,[31] A. Stocchi,[31] L. L. Wang,[31,§] G. Wormser,[31] D. J. Lange,[32] D. M. Wright,[32] J. P. Coleman,[33] J. R. Fry,[33] E. Gabathuler,[33] D. E. Hutchcroft,[33] D. J. Payne,[33] C. Touramanis,[33] A. J. Bevan,[34] F. Di Lodovico,[34] R. Sacco,[34] G. Cowan,[35] D. N. Brown,[36] C. L. Davis,[36] A. G. Denig,[37] M. Fritsch,[37] W. Gradl,[37] K. Griessinger,[37] A. Hafner,[37] K. R. Schubert,[37] R. J. Barlow,[38,¶] G. D. Lafferty,[38] R. Cenci,[39] B. Hamilton,[39] A. Jawahery,[39] D. A. Roberts,[39] R. Cowan,[40] R. Cheaib,[41] P. M. Patel,[41,*] S. H. Robertson,[41] N. Neri,[42a] F. Palombo,[42a,42b] L. Cremaldi,[43] R. Godang,[43,**] D. J. Summers,[43] M. Simard,[44] P. Taras,[44] G. De Nardo,[45a,45b] G. Onorato,[45a,45b] C. Sciacca,[45a,45b] G. Raven,[46] C. P. Jessop,[47] J. M. LoSecco,[47] K. Honscheid,[48] R. Kass,[48] M. Margoni,[49a,49b] M. Morandin,[49a] M. Posocco,[49a] M. Rotondo,[49a] G. Simi,[49a,49b] F. Simonetto,[49a,49b] R. Stroili,[49a,49b] S. Akar,[50] E. Ben-Haim,[50] M. Bomben,[50] G. R. Bonneaud,[50] H. Briand,[50] G. Calderini,[50] J. Chauveau,[50] Ph. Leruste,[50] G. Marchiori,[50] J. Ocariz,[50] M. Biasini,[51a,51b] E. Manoni,[51a] A. Rossi,[51a] C. Angelini,[52a,52b] G. Batignani,[52a,52b] S. Bettarini,[52a,52b] M. Carpinelli,[52a,52b,††] G. Casarosa,[52a,52b] M. Chrzaszcz,[52a] F. Forti,[52a,52b] M. A. Giorgi,[52a,52b] A. Lusiani,[52a,52c] B. Oberhof,[52a,52b] E. Paoloni,[52a,52b] M. Rama,[52a] G. Rizzo,[52a,52b] J. J. Walsh,[52a] D. Lopes Pegna,[53] J. Olsen,[53] A. J. S. Smith,[53] F. Anulli,[54a] R. Faccini,[54a,54b] F. Ferrarotto,[54a] F. Ferroni,[54a,54b] M. Gaspero,[54a,54b] A. Pilloni,[54a,54b] G. Piredda,[54a] C. Bünger,[55] S. Dittrich,[55] O. Grünberg,[55] M. Hess,[55] T. Leddig,[55] C. Voß,[55] R. Waldi,[55] T. Adye,[56] E. O. Olaiya,[56] F. F. Wilson,[56] S. Emery,[57] G. Vasseur,[57] D. Aston,[58] D. J. Bard,[58] C. Cartaro,[58] M. R. Convery,[58] J. Dorfan,[58] G. P. Dubois-Felsmann,[58] W. Dunwoodie,[58] M. Ebert,[58] R. C. Field,[58] B. G. Fulsom,[58] M. T. Graham,[58] C. Hast,[58] W. R. Innes,[58] P. Kim,[58] D. W. G. S. Leith,[58] S. Luitz,[58] V. Luth,[58] D. B. MacFarlane,[58] D. R. Muller,[58] H. Neal,[58] T. Pulliam,[58] B. N. Ratcliff,[58] A. Roodman,[58] R. H. Schindler,[58] A. Snyder,[58] D. Su,[58] M. K. Sullivan,[58] J. Va'vra,[58] W. J. Wisniewski,[58] H. W. Wulsin,[58] M. V. Purohit,[59] J. R. Wilson,[59] A. Randle-Conde,[60] S. J. Sekula,[60] M. Bellis,[61] P. R. Burchat,[61] E. M. T. Puccio,[61] M. S. Alam,[62] J. A. Ernst,[62] R. Gorodeisky,[63] N. Guttman,[63] D. R. Peimer,[63] A. Soffer,[63] S. M. Spanier,[64] J. L. Ritchie,[65] R. F. Schwitters,[65] J. M. Izen,[66] X. C. Lou,[66] F. Bianchi,[67a,67b] F. De Mori,[67a,67b] A. Filippi,[67a] D. Gamba,[67a,67b] L. Lanceri,[68a,68b] L. Vitale,[68a,68b] F. Martinez-Vidal,[69] A. Oyanguren,[69] J. Albert,[70] Sw. Banerjee,[70] A. Beaulieu,[70] F. U. Bernlochner,[70] H. H. F. Choi,[70] G. J. King,[70] R. Kowalewski,[70] M. J. Lewczuk,[70] T. Lueck,[70] I. M. Nugent,[70] J. M. Roney,[70] R. J. Sobie,[70] N. Tasneem,[70] T. J. Gershon,[71] P. F. Harrison,[71] T. E. Latham,[71] H. R. Band,[72] S. Dasu,[72] Y. Pan,[72] R. Prepost,[72] and S. L. Wu[72]

(The *BABAR* Collaboration)

[1]*Laboratoire d'Annecy-le-Vieux de Physique des Particules (LAPP), Université de Savoie, CNRS/IN2P3, F-74941 Annecy-Le-Vieux, France*
[2]*Universitat de Barcelona, Facultat de Fisica, Departament ECM, E-08028 Barcelona, Spain*
[3a]*INFN Sezione di Bari, I-70126 Bari, Italy*
[3b]*Dipartimento di Fisica, Università di Bari, I-70126 Bari, Italy*
[4]*University of Bergen, Institute of Physics, N-5007 Bergen, Norway*
[5]*Lawrence Berkeley National Laboratory and University of California, Berkeley, California 94720, USA*
[6]*Ruhr Universität Bochum, Institut für Experimentalphysik 1, D-44780 Bochum, Germany*
[7]*University of British Columbia, Vancouver, British Columbia, Canada V6T 1Z1*
[8]*Brunel University, Uxbridge, Middlesex UB8 3PH, United Kingdom*
[9a]*Budker Institute of Nuclear Physics SB RAS, Novosibirsk 630090, Russia*
[9b]*Novosibirsk State University, Novosibirsk 630090, Russia*
[9c]*Novosibirsk State Technical University, Novosibirsk 630092, Russia*

[10]*University of California at Irvine, Irvine, California 92697, USA*
[11]*University of California at Riverside, Riverside, California 92521, USA*
[12]*University of California at Santa Barbara, Santa Barbara, California 93106, USA*
[13]*University of California at Santa Cruz, Institute for Particle Physics, Santa Cruz, California 95064, USA*
[14]*California Institute of Technology, Pasadena, California 91125, USA*
[15]*University of Cincinnati, Cincinnati, Ohio 45221, USA*
[16]*University of Colorado, Boulder, Colorado 80309, USA*
[17]*Colorado State University, Fort Collins, Colorado 80523, USA*
[18]*Technische Universität Dortmund, Fakultät Physik, D-44221 Dortmund, Germany*
[19]*Laboratoire Leprince-Ringuet, Ecole Polytechnique, CNRS/IN2P3, F-91128 Palaiseau, France*
[20]*University of Edinburgh, Edinburgh EH9 3JZ, United Kingdom*
[21a]*INFN Sezione di Ferrara, I-44122 Ferrara, Italy*
[21b]*Dipartimento di Fisica e Scienze della Terra, Università di Ferrara, I-44122 Ferrara, Italy*
[22]*INFN Laboratori Nazionali di Frascati, I-00044 Frascati, Italy*
[23a]*INFN Sezione di Genova, I-16146 Genova, Italy*
[23b]*Dipartimento di Fisica, Università di Genova, I-16146 Genova, Italy*
[24]*Indian Institute of Technology Guwahati, Guwahati, Assam, 781 039, India*
[25]*Universität Heidelberg, Physikalisches Institut, D-69120 Heidelberg, Germany*
[26]*Humboldt-Universität zu Berlin, Institut für Physik, D-12489 Berlin, Germany*
[27]*University of Iowa, Iowa City, Iowa 52242, USA*
[28]*Iowa State University, Ames, Iowa 50011-3160, USA*
[29]*Physics Department, Jazan University, Jazan 22822, Kingdom of Saudi Arabia*
[30]*Johns Hopkins University, Baltimore, Maryland 21218, USA*
[31]*Laboratoire de l'Accélérateur Linéaire, IN2P3/CNRS et Université Paris-Sud 11, Centre Scientifique d'Orsay, F-91898 Orsay Cedex, France*
[32]*Lawrence Livermore National Laboratory, Livermore, California 94550, USA*
[33]*University of Liverpool, Liverpool L69 7ZE, United Kingdom*
[34]*Queen Mary, University of London, London E1 4NS, United Kingdom*
[35]*University of London, Royal Holloway and Bedford New College, Egham, Surrey TW20 0EX, United Kingdom*
[36]*University of Louisville, Louisville, Kentucky 40292, USA*
[37]*Johannes Gutenberg-Universität Mainz, Institut für Kernphysik, D-55099 Mainz, Germany*
[38]*University of Manchester, Manchester M13 9PL, United Kingdom*
[39]*University of Maryland, College Park, Maryland 20742, USA*
[40]*Massachusetts Institute of Technology, Laboratory for Nuclear Science, Cambridge, Massachusetts 02139, USA*
[41]*McGill University, Montréal, Québec, Canada H3A 2T8*
[42a]*INFN Sezione di Milano, I-20133 Milano, Italy*
[42b]*Dipartimento di Fisica, Università di Milano, I-20133 Milano, Italy*
[43]*University of Mississippi, University, Mississippi 38677, USA*
[44]*Université de Montréal, Physique des Particules, Montréal, Québec, Canada H3C 3J7*
[45a]*INFN Sezione di Napoli, I-80126 Napoli, Italy*
[45b]*Dipartimento di Scienze Fisiche, Università di Napoli Federico II, I-80126 Napoli, Italy*
[46]*NIKHEF, National Institute for Nuclear Physics and High Energy Physics, NL-1009 DB Amsterdam, The Netherlands*
[47]*University of Notre Dame, Notre Dame, Indiana 46556, USA*
[48]*Ohio State University, Columbus, Ohio 43210, USA*
[49a]*INFN Sezione di Padova, I-35131 Padova, Italy*
[49b]*Dipartimento di Fisica, Università di Padova, I-35131 Padova, Italy*
[50]*Laboratoire de Physique Nucléaire et de Hautes Energies, IN2P3/CNRS, Université Pierre et Marie Curie-Paris6, Université Denis Diderot-Paris7, F-75252 Paris, France*
[51a]*INFN Sezione di Perugia, I-06123 Perugia, Italy*
[51b]*Dipartimento di Fisica, Università di Perugia, I-06123 Perugia, Italy*
[52a]*INFN Sezione di Pisa, I-56127 Pisa, Italy*
[52b]*Dipartimento di Fisica, Università di Pisa, I-56127 Pisa, Italy*
[52c]*Scuola Normale Superiore di Pisa, I-56127 Pisa, Italy*
[53]*Princeton University, Princeton, New Jersey 08544, USA*
[54a]*INFN Sezione di Roma, I-00185 Roma, Italy*
[54b]*Dipartimento di Fisica, Università di Roma La Sapienza, I-00185 Roma, Italy*
[55]*Universität Rostock, D-18051 Rostock, Germany*

[56]Rutherford Appleton Laboratory, Chilton, Didcot, Oxon OX11 0QX, United Kingdom
[57]CEA, Irfu, SPP, Centre de Saclay, F-91191 Gif-sur-Yvette, France
[58]SLAC National Accelerator Laboratory, Stanford, California 94309 USA
[59]University of South Carolina, Columbia, South Carolina 29208, USA
[60]Southern Methodist University, Dallas, Texas 75275, USA
[61]Stanford University, Stanford, California 94305-4060, USA
[62]State University of New York, Albany, New York 12222, USA
[63]Tel Aviv University, School of Physics and Astronomy, Tel Aviv, 69978, Israel
[64]University of Tennessee, Knoxville, Tennessee 37996, USA
[65]University of Texas at Austin, Austin, Texas 78712, USA
[66]University of Texas at Dallas, Richardson, Texas 75083, USA
[67a]INFN Sezione di Torino, I-10125 Torino, Italy
[67b]Dipartimento di Fisica, Università di Torino, I-10125 Torino, Italy
[68a]INFN Sezione di Trieste, I-34127 Trieste, Italy
[68b]Dipartimento di Fisica, Università di Trieste, I-34127 Trieste, Italy
[69]IFIC, Universitat de Valencia-CSIC, E-46071 Valencia, Spain
[70]University of Victoria, Victoria, British Columbia, Canada V8W 3P6
[71]Department of Physics, University of Warwick, Coventry CV4 7AL, United Kingdom
[72]University of Wisconsin, Madison, Wisconsin 53706, USA
(Received 1 September 2015; published 28 October 2015)

Charge asymmetry in the processes $e^+e^- \to \mu^+\mu^-\gamma$ and $e^+e^- \to \pi^+\pi^-\gamma$ is measured using 232 fb^{-1} of data collected with the *BABAR* detector at e^+e^- center-of-mass energies near 10.58 GeV. An observable is introduced and shown to be very robust against detector asymmetries while keeping a large sensitivity to the physical charge asymmetry that results from the interference between initial- and final-state radiation (FSR). The asymmetry is determined as a function of the invariant mass of the final-state tracks from production threshold to a few GeV$/c^2$. It is compared to the expectation from QED for $e^+e^- \to \mu^+\mu^-\gamma$, and from theoretical models for $e^+e^- \to \pi^+\pi^-\gamma$. A clear interference pattern is observed in $e^+e^- \to \pi^+\pi^-\gamma$, particularly in the vicinity of the $f_2(1270)$ resonance. The inferred rate of lowest-order FSR production is consistent with the QED expectation for $e^+e^- \to \mu^+\mu^-\gamma$, and is negligibly small for $e^+e^- \to \pi^+\pi^-\gamma$.

DOI: 10.1103/PhysRevD.92.072015 PACS numbers: 13.60.Hb, 13.66.Bc, 13.66.Jn

I. INTRODUCTION

The radiative processes

$$e^+e^- \to X\gamma \tag{1}$$

have been extensively studied by several e^+e^- experiments and the cross sections for $e^+e^- \to X$ have been measured using the initial-state radiation (ISR) method [1–4]. At *BABAR* [5], the cross sections have thus been determined in large energy ranges below the total e^+e^- center-of-mass (c.m.) energy $\sqrt{s} \sim 10.58\,\text{GeV}$ available at the SLAC PEP-II collider. The state X can be either fully described by quantum electrodynamics (QED) such as $\mu^+\mu^-$, or any hadronic state with $J^{PC} = 1^{--}$.

In reaction (1) at lowest order (LO) the photon can be emitted from either the incoming electron or positron, or from the final state (final-state radiation, or FSR). At *BABAR*, the kinematic conditions are such that the process is dominated by ISR photons, which justifies the ISR method. The LO FSR contribution to the hadronic radiative process is neglected, as its theoretical estimates are well below the systematic uncertainties of the cross section measurement. This is due to the fact that the available e^+e^- c.m. energy is far beyond the domain of the hadronic resonances that dominate the cross section, so that hadronic form factors considerably reduce the probability that the photon is emitted from the final state. However, the theoretical estimations are model dependent, and it is thus important to have a direct experimental proof of the smallness of the FSR contribution to the hadronic cross sections when high precision is at stake, as for the determination of the hadronic contribution to the $g-2$ value of the muon [6]. Because of the point-like nature of the muon, the FSR reduction does not occur for the $e^+e^- \to \mu^+\mu^-\gamma$ process. The LO FSR contribution to the cross section is expected to vanish at threshold and to increase

[*]Deceased.
[†]Now at: University of Tabuk, Tabuk 71491, Saudi Arabia.
[‡]Now at: Laboratoire de Physique Nucléaire et de Hautes Energies, IN2P3/CNRS, F-75252 Paris, France.
[§]Now at: Institute of High Energy Physics, Beijing 100049, China.
[¶]Now at: University of Huddersfield, Huddersfield HD1 3DH, United Kingdom.
[**]Now at: University of South Alabama, Mobile, Alabama 36688, USA.
[††]Also at: Università di Sassari, I-07100 Sassari, Italy.

with the invariant mass of the muon pair ($m_{\mu\mu}$). Still, the FSR fraction remains small for low di-muon mass (less than 1% for $m_{\mu\mu} < 1\,\mathrm{GeV}/c^2$). For the $e^+e^- \to \mu^+\mu^-\gamma$ cross section measurement, a correction is applied for the LO FSR contribution as a function of $m_{\mu\mu}$, which is so far determined by turning off FSR in the Monte Carlo (MC) generation.

While it is not possible to distinguish ISR from FSR photons on an event-by-event basis, as the corresponding amplitudes are both present and interfere, a measurement of the interference provides a sensitive and quantitative determination of their relative strength. Measurement of the forward-backward asymmetry of the pions was first proposed in Ref. [3], as a test of the underlying model for final-state radiation. In this paper, the ISR-FSR interference for $e^+e^- \to \mu^+\mu^-\gamma$ and $e^+e^- \to \pi^+\pi^-\gamma$ is studied through the charge asymmetry of the production of these events at various decay plane angles. The comparison between the QED prediction and the measurement is done for the charge asymmetry in $e^+e^- \to \mu^+\mu^-\gamma$. Various FSR models are discussed for $e^+e^- \to \pi^+\pi^-\gamma$, and the most realistic quark-FSR model is compared to the measurement of the charge asymmetry in that channel.

This paper reports the first measurement of charge asymmetry in the $e^+e^- \to \mu^+\mu^-\gamma$ process. For $e^+e^- \to \pi^+\pi^-\gamma$, a preliminary measurement [7] of the forward-backward asymmetry has been reported at low energies ($\sqrt{s} \sim 1\,\mathrm{GeV}$). No previous result exists at high energies.

II. ISR-FSR INTERFERENCE AND CHARGE ASYMMETRY

A. Charge asymmetry

The Feynman diagrams for the LO ISR and LO FSR emission in the process $e^+e^- \to x^+x^-\gamma$ (where $x = \mu$ or π), are illustrated in Fig. 1. The total LO amplitude $\mathcal{M}$ is the sum of the corresponding amplitudes $\mathcal{M}_{\mathrm{ISR}}$ and $\mathcal{M}_{\mathrm{FSR}}$, and the cross section for $e^+e^- \to x^+x^-\gamma$ is

$$\sigma \propto |\mathcal{M}|^2 = |\mathcal{M}_{\mathrm{ISR}}|^2 + |\mathcal{M}_{\mathrm{FSR}}|^2 + 2\mathcal{R}e(\mathcal{M}_{\mathrm{ISR}}\mathcal{M}^*_{\mathrm{FSR}}). \tag{2}$$

If the photon is emitted from the initial (final) state, the x^+x^- pair is produced with charge parity $C = -1(+1)$, which implies that the interference term changes sign if one interchanges x^+ and x^-. While the contribution of the interference term to the total cross section vanishes when one integrates over the kinematic variables of the final state, that term induces a significant observable charge asymmetry in the differential cross section.

Charge asymmetry is defined as

$$\mathcal{A} = \frac{|\mathcal{M}|^2 - |\mathcal{M}_{x^+\leftrightarrow x^-}|^2}{|\mathcal{M}|^2 + |\mathcal{M}_{x^+\leftrightarrow x^-}|^2} = \frac{2\mathcal{R}e(\mathcal{M}_{\mathrm{ISR}}\mathcal{M}^*_{\mathrm{FSR}})}{|\mathcal{M}_{\mathrm{ISR}}|^2 + |\mathcal{M}_{\mathrm{FSR}}|^2}, \tag{3}$$

where $x^+ \leftrightarrow x^-$ means that x^+ and x^- are interchanged.

Although it is not possible to reconstruct $\mathcal{M}_{\mathrm{ISR}}$ or $\mathcal{M}_{\mathrm{FSR}}$ from the charge asymmetry and the cross section, as the relative phase between them remains unknown, information on the ratio $|\mathcal{M}_{\mathrm{FSR}}/\mathcal{M}_{\mathrm{ISR}}|$ can be derived within the framework of specific models.

B. Choice of kinematic variables

Aside from an overall azimuthal rotation about the beam axis, the kinematic topology of the $x^+x^-\gamma$ final state (where $x = \mu$ or π) is described by four variables, which are the muon-pair (pion-pair) invariant mass m_{xx} (or equivalently E^*_γ, the energy of the radiated photon in the e^+e^- c.m.) and three angular variables. At a given m_{xx} mass, the distribution of the three angular variables contains all the available information on the ISR/FSR amplitudes.

At variance with the definition of forward-backward asymmetry used in Ref. [8], which refers to the polar angle of x^- with respect to the incoming electron in the e^+e^- c.m. system (c.m.s.), this analysis introduces the set of angular variables illustrated in Fig. 2. These are found to be more sensitive observables to measure the ISR-FSR interference:

(i) θ^*_γ—polar angle of the radiated photon in the e^+e^- c.m.s. (with respect to the e^+e^- axis);
(ii) θ^*—polar angle of x^- with respect to the photon axis in the x^+x^- c.m.s.;
(iii) ϕ^*—azimuthal angle of x^- with respect to the γe^+e^- plane in the x^+x^- c.m.s. (or the e^+e^- c.m.s.).

Since $x^+ \leftrightarrow x^-$ interchange means reversal of the x^- direction to its opposite in the x^+x^- c.m.s., the charge asymmetry, for fixed m_{xx} and θ^*_γ, is equal to

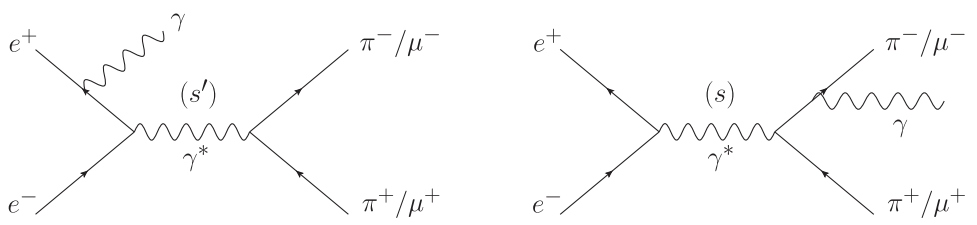

FIG. 1. Feynman diagrams for $e^+e^- \to x^+x^-\gamma$ ($x = \mu, \pi$), where the photon is from LO ISR (left) or LO FSR (right).

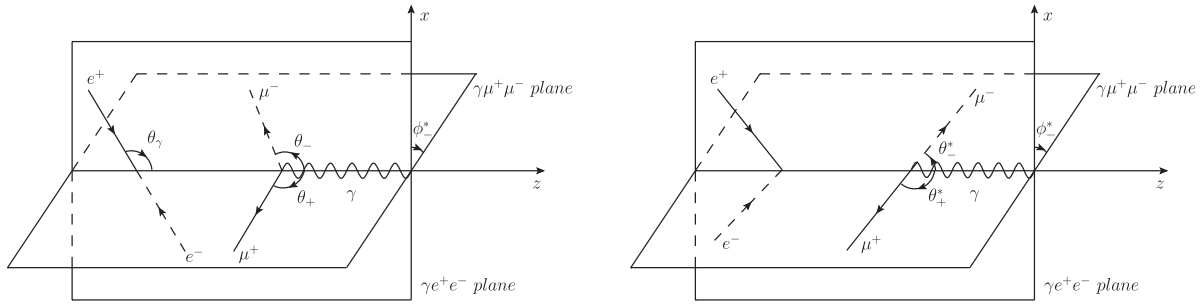

FIG. 2. Definition of the angular variables describing the kinematic topology of the final states of the process $e^+e^- \to x^+x^-\gamma$ $(x = \mu, \pi)$ at a given x^+x^- invariant mass (left) in the e^+e^- c.m.s., and (right) in the x^+x^- c.m.s.

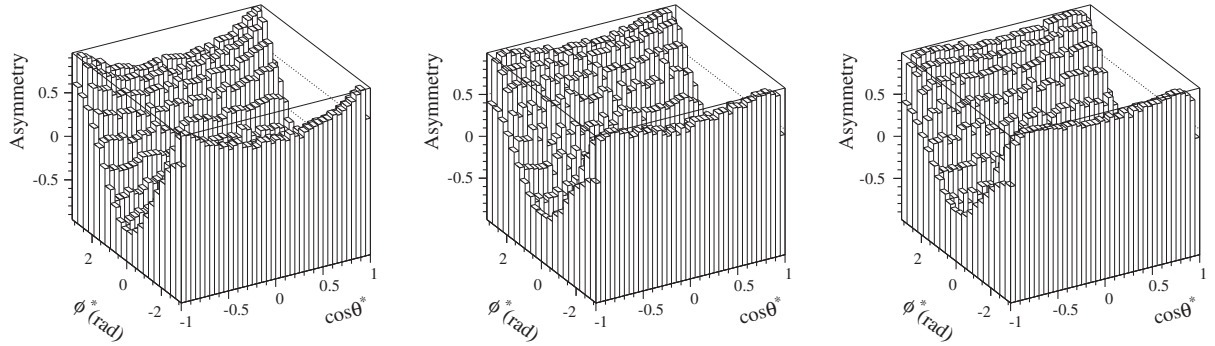

FIG. 3. Charge asymmetry at generator level in $e^+e^- \to \mu^+\mu^-\gamma$ simulation, as a function of $\cos\theta^*$ and ϕ^* for the same $m_{\mu\mu}$ interval $(6.5 < m_{\mu\mu} < 7.0\,\mathrm{GeV}/c^2)$ and various $\cos\theta^*_\gamma$ ranges: (left) $-1 < \cos\theta^*_\gamma < -0.6$, (middle) $-0.6 < \cos\theta^*_\gamma < -0.4$, (right) $-0.4 < \cos\theta^*_\gamma < 0$.

$$\mathcal{A}(\theta^*, \phi^*) = \frac{\sigma(\theta^*, \phi^*) - \sigma(\pi - \theta^*, \pi + \phi^*)}{\sigma(\theta^*, \phi^*) + \sigma(\pi - \theta^*, \pi + \phi^*)}. \quad (4)$$

For the $e^+e^- \to \mu^+\mu^-\gamma$ process, the charge asymmetry as a function of $\cos\theta^*$ and ϕ^*, studied with the AFKQED generator (see Sec. IV B), is shown in Fig. 3. The FSR amplitude is dominant at $|\cos\theta^*| \sim 1$, when one of the charged-particle tracks is very close to the radiated photon. However, Fig. 3 shows that ϕ^* is a more sensitive variable to measure the ISR/FSR content over the full phase space, with sign reversal of the charge asymmetry. After integration over $\cos\theta^*_\gamma$ and integration over symmetrical $\cos\theta^*$ intervals, the distribution of the integrated charge asymmetry $A(\cos\phi^*)$ suggests a simple linear dependence

$$A(\cos\phi^*) = A_0 \cos\phi^*. \quad (5)$$

From the expressions of the differential cross section detailed in the next section, it results that the slope A_0 is an estimator of the ISR-FSR interference, sensitive to the ratio $|\mathcal{M}_{\mathrm{FSR}}/\mathcal{M}_{\mathrm{ISR}}|$ in each $m_{\mu\mu}$ interval. Moreover, it will be shown in Sec. V that the measurement of A_0 is barely affected by detector charge asymmetries.

III. THEORETICAL PREDICTIONS FOR THE CHARGE ASYMMETRY

A. QED prediction for the $e^+e^- \to \mu^+\mu^-\gamma$ process

In the massless limit [9], the differential cross section of the QED $e^+e^- \to \mu^+\mu^-\gamma$ process, written as a function of the four kinematic variables defined above (Sec. II B), implies that the differential charge asymmetry is proportional to $\cos\phi^*$:

$$\mathcal{A}_{e^+e^-\to\mu^+\mu^-\gamma}(m_{\mu\mu}, \theta^*_\gamma, \theta^*, \phi^*) = -\frac{2\sqrt{s}\, m_{\mu\mu} \sin\theta^*_\gamma \sin\theta^* \cos\phi^*}{s\sin^2\theta^* + m^2_{\mu\mu}\sin^2\theta^*_\gamma}. \quad (6)$$

When the masses are taken into account, the effect from the electron/positron mass is found to be negligible for radiated photons away from the beams. The effect from the muon mass is sizable, especially at large $m_{\mu\mu}$ when the radiated photon is close to one of the muons. Predictions for the charge asymmetry in the massive case are obtained by numerical integration of several variants of the QED differential cross section [9–11]. The phase space considered in those calculations is limited to the experimental acceptance $20° < \theta^*_\gamma < 160°$, and the results are shown in

Fig. 4 as a function of $m_{\mu\mu}$. Predictions differ at the physical threshold ($m_{\mu\mu} = 2m_\mu$), where only the charge asymmetry based on Ref. [11] extrapolates to zero as expected, suggesting that the validity of formulas in Refs. [9,10] does not extend to small $m_{\mu\mu}$. At large mass ($m_{\mu\mu} > 3\,\mathrm{GeV}/c^2$), the prediction from Ref. [9] differs from the others by up to a few percent. The formula of the differential LO cross section implemented in the AFKQED generator, which is used in this analysis for simulation (see Sec. IV B), is the one by Arbuzov *et al.* [11], which has the most reliable behavior over the full $m_{\mu\mu}$ range.

B. FSR models for the $e^+e^- \to \pi^+\pi^-\gamma$ process

As in the $e^+e^- \to \mu^+\mu^-\gamma$ process, ISR and FSR contribute to $e^+e^- \to \pi^+\pi^-\gamma$ (Fig. 5). However, the charge asymmetry is expected to be much smaller in the latter process because the FSR contribution is strongly reduced by the pion form factor at large $\sqrt{s}$. In addition, its estimate is model dependent.

1. FSR from point-like pions (model 1)

In the FSR model shown in Fig. 5(b), the photon is emitted from one of the final-state pions, where the pion is treated as a point-like particle. In this hypothesis, the FSR amplitude $\mathcal{M}_{\mathrm{FSR}}$ is proportional to the pion form factor at the collision energy squared s, namely $F_\pi(s)$. The ISR amplitude $\mathcal{M}_{\mathrm{ISR}}$ shown in Fig. 5(a) is proportional to the pion form factor $F_\pi(s')$ at a reduced energy squared $s' = s(1 - 2E^*_\gamma/\sqrt{s})$. According to this FSR model, the charge asymmetry to be measured at *BABAR* reflects the relative magnitude of the pion form factor at $\sqrt{s} = 10.58\,\mathrm{GeV}$ and at low energy. It is consequently negligibly small, since $F_\pi(s')$, dominated by the ρ resonance in the $s' = m^2_{\pi\pi}$ domain accessible to the experiment, is 3 orders of magnitude larger than $|F_\pi(10.58^2\,\mathrm{GeV}^2)| \sim 0.01$, as estimated from an extrapolation of existing data [6,12] using a $1/s$ dependence. This model is studied with the PHOKHARA 4.0 [13] generator, in which the FSR current has a point-like Lorentz structure, including a contact term,

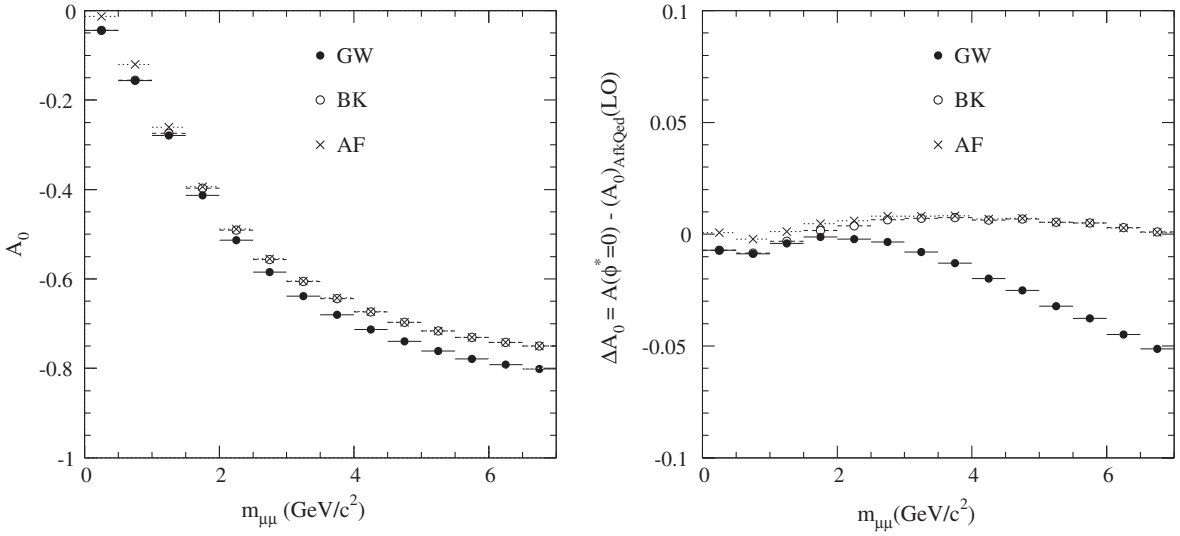

FIG. 4. (Left) Charge asymmetry at $\phi^* = 0$, A_0, as a function of $m_{\mu\mu}$, obtained by numerical integration according to three different theoretical predictions (see text), with the condition $20° < \theta^*_\gamma < 160°$ applied. (Right) The difference between the prediction and the AFKQED LO value. Results labeled GW, BK, AF are obtained from Refs. [9–11], respectively.

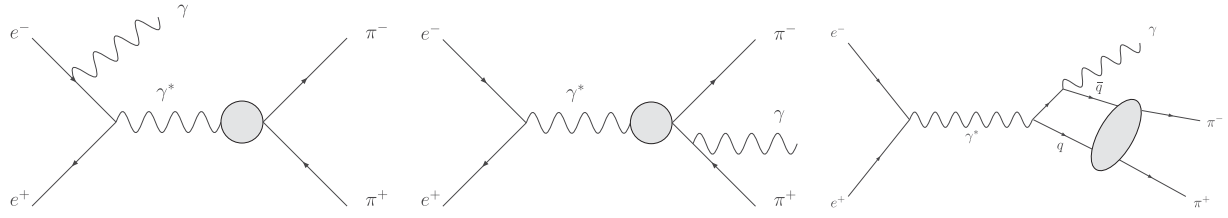

FIG. 5. Feynman diagrams for $e^+e^- \to \pi^+\pi^-\gamma$. (a) Initial state radiation, (b) Final state radiation with pions treated as point-like particles (FSR model 1), (c) Final state radiation at quark level (FSR model 2).

globally multiplied by the pion form factor. In this model, the $A_0(m_{\pi\pi})$ distribution is expected to increase quadratically with mass on the ρ resonance, with a change of sign at the ρ mass

$$A_0 \sim 2 \times 10^{-3}(m^2_{\pi\pi} - m^2_\rho), \tag{7}$$

with values well below the sensitivity of this analysis because of the large pion form factor suppression at 10.58 GeV.

2. FSR from quarks (model 2)

In the *a priori* more realistic FSR model for $e^+e^- \to \pi^+\pi^-\gamma$ depicted in Fig. 5(c), the FSR photon is emitted from the quarks, which subsequently hadronize into a pion pair [14]. The dominant ISR[1] and FSR contributions, and their interference, are written in terms of the variables defined in Sec. II B:

$$\begin{aligned}\frac{d\sigma^{\rm ISR}_{e^+e^-\to\pi^+\pi^-\gamma}}{dm^2_{\pi\pi}d\cos\theta^*_\gamma d\cos\theta^* d\phi^*} &= \frac{\alpha^3\beta^3}{16\pi s^2 m^2_{\pi\pi}(s-m^2_{\pi\pi})}|F_\pi(m^2_{\pi\pi})|^2 \\ &\times\left\{(s^2+m^4_{\pi\pi})\frac{1+\cos^2\theta^*_\gamma}{\sin^2\theta^*_\gamma}\sin^2\theta^* + 4sm^2_{\pi\pi}\cos^2\theta^* \right. \\ &- 2\sqrt{s}m_{\pi\pi}(s+m^2_{\pi\pi})(\tan\theta^*_\gamma)^{-1}\sin 2\theta^*\cos\phi^* \\ &\left. - 2sm^2_{\pi\pi}\sin^2\theta^*\cos 2\phi^*\right\},\end{aligned} \tag{8}$$

where α and β are the QED fine-structure constant and the pion velocity $\beta = \sqrt{1-4m^2_\pi/m^2_{\pi\pi}}$, respectively. The FSR contribution is

$$\begin{aligned}\frac{d\sigma^{\rm FSR}_{e^+e^-\to\pi^+\pi^-\gamma}}{dm^2_{\pi\pi}d\cos\theta^*_\gamma d\cos\theta^* d\phi^*} &= \frac{\alpha^3\beta(s-m^2_{\pi\pi})}{64\pi s^3}(1+\cos^2\theta^*_\gamma)|V(m^2_{\pi\pi},\theta^*)|^2,\end{aligned} \tag{9}$$

and the interference term

$$\begin{aligned}\frac{d\sigma^{I}_{e^+e^-\to\pi^+\pi^-\gamma}}{dm^2_{\pi\pi}d\cos\theta^*_\gamma d\cos\theta^* d\phi^*} &= \frac{\alpha^3\beta^2}{16\pi s^2\sqrt{s}m_{\pi\pi}}{\rm Re}\{F^*_\pi(m^2_{\pi\pi})V(m^2_{\pi\pi},\theta^*)\} \\ &\times\left\{-\sqrt{s}m_{\pi\pi}\cos\theta^*_\gamma\cos\theta^* + [(1+\cos^2\theta^*_\gamma)s\right. \\ &\left. + m^2_{\pi\pi}\sin^2\theta^*_\gamma]\frac{\sin\theta^*\cos\phi^*}{2\sin\theta^*_\gamma}\right\},\end{aligned} \tag{10}$$

where

$$\begin{aligned}V = \sum_q e^2_q V_q = \sum_q e^2_q\int_0^1 dz\frac{2z-1}{z(1-z)}\Phi^+_q(z,m^2_{\pi\pi},\cos\theta^*) \\ (q=u,d),\end{aligned} \tag{11}$$

and $\Phi^+_q(z,m^2_{\pi\pi},\cos\theta^*)$ is the C-even part of the two-pion generalized distribution amplitudes (GDA). The pion time-like form factor $F_\pi(m^2_{\pi\pi})$ is taken from a fit to *BABAR* data [6] with a vector dominance model.

So far, there is no implementation of this model in an MC generator to describe the ISR-FSR interference in the $e^+e^- \to \pi^+\pi^-\gamma$ process. In order to predict the charge asymmetry numerically, we take the following GDA model, which is a modified version of the model found in Ref. [16]:

$$\begin{aligned}\Phi^+_u(z,m^2_{\pi\pi},\cos\theta^*) &= \Phi^+_d(z,m^2_{\pi\pi},\cos\theta^*) \\ &= 10z(1-z)(2z-1) \\ &\times\left[c_0\frac{3-\beta^2}{2}e^{i\delta_0(m_{\pi\pi})} + c_2\beta^2{\rm BW}(m_{\pi\pi})P_2(\cos\theta^*)\right],\end{aligned} \tag{12}$$

where c_0 and c_2 are the magnitudes of the S-wave and D-wave contributions, respectively. As the scalar sector is known to involve wide resonances, the S-wave contribution is approximated by a constant amplitude with a mass-dependent phase $\delta_0(m_{\pi\pi})$ taken from pion-pion phase-shift analyses [17] in the region below $1.6\,{\rm GeV}/c^2$. This model incorporates the rapid phase variation across the $f_0(980)$ resonance. Using $c_0 = -0.5$ [16] yields an A_0 value of about -1% near the ρ resonance and nearly flat with mass. For the D-wave tensor contribution, we use a Breit-Wigner (BW) form for the $f_2(1270)$ resonance in order to take properly into account the mass dependence of the amplitude, the phase variation being given by the BW form in agreement with the measured $\delta_2(m_{\pi\pi})$ values [17]. The angular dependence in the $\pi\pi$ center of mass is given by the Legendre polynomial $P_2(\cos\theta^*)$, which assumes the dominance of helicity 0 for $f_2(1270)$ production.

[1]We thank Leonard Lesniak for pointing out a sign mistake in the $\sin 2\theta^*\cos\phi^*$ term of Eq. (8) as given in the erratum of Ref. [14]. The correct sign has been checked with the formulas given in Ref. [15].

C. Other sources of charge asymmetry

Next-to-leading-order (NLO) corrections including additional photons (soft and hard) and loops are expected to affect the LO predictions for the charge asymmetry. For the $\mu^+\mu^-\gamma$ process these corrections have been computed recently [18] and implemented in the PHOKHARA 9.0 generator [18]. As discussed in Sec. VI C, the effects are found to be small, at the percent level for the experimental conditions of the present analysis, and to be well accounted for by the simpler structure function approach implemented in AFKQED. No exact NLO calculation is available for the $\pi^+\pi^-\gamma$ process. In this case, since the LO charge asymmetry is expected to be small because the FSR amplitude is suppressed, NLO corrections could play a relatively more important role. The soft and virtual photon contributions to the Born process $e^+e^- \to \pi^+\pi^-$ are known [15,19] to generate an asymmetry of the pion production, with asymmetry values at the percent level at a $\pi\pi$ mass of $1\,\mathrm{GeV}/c^2$. However, it is unclear if the above result can be used in the conditions of the present process $e^+e^- \to \pi^+\pi^-\gamma$, where one of the incoming electrons is highly off shell after emission of a hard ISR photon. Furthermore, such an asymmetry would vanish because of the symmetrical integration in $\cos\theta^*$. NLO corrections as implemented in AFKQED have indeed no effect on the charge asymmetry. No correction on the measured charge asymmetry is therefore applied for the $\pi^+\pi^-\gamma$ process.

Another potential source of charge asymmetry comes from Z exchange. This contribution is strongly suppressed by the Z propagator, especially for the ISR diagrams where $m_{xx}^2/M_Z^2 \sim 10^{-4}$. Therefore one expects this effect to be negligible for $\pi^+\pi^-\gamma$. The contribution is larger for the FSR diagrams for $\mu^+\mu^-\gamma$ since here the relevant ratio is $s/M_Z^2 = 1.4\%$. The contribution of Z exchange is studied with the KKMC generator [20]. As reported in Sec. VI C, the effect is at the level of a few per mille.

IV. EXPERIMENTAL ANALYSIS

A. The *BABAR* detector and data samples

The analysis is based on 232 fb^{-1} of data [21] collected with the *BABAR* detector at the SLAC National Accelerator Laboratory at the PEP-II asymmetric-energy e^+e^- collider operated at the $\Upsilon(4S)$ resonance. About 10% of the data was collected 40 MeV below the resonance. The *BABAR* detector is described in detail elsewhere [22]. Charged-particle tracks are measured with a five-layer double-sided silicon vertex tracker (SVT) together with a 40-layer drift chamber (DCH), both inside a 1.5 T superconducting solenoid. Photons are assumed to originate from the primary vertex defined by the charged-particle tracks of the event, and their energy and position are measured in a CsI(Tl) electromagnetic calorimeter (EMC). Charged-particle identification (PID) uses the ionization energy loss $\mathrm{d}E/\mathrm{d}x$ in the SVT and DCH, the Cherenkov radiation detected in a ring-imaging device (DIRC), the shower energy deposit (E_{cal}) in the EMC, and the shower shape in the instrumented flux return (IFR) of the magnet. The IFR system is made of modules of resistive plate chambers interspaced with iron slabs, arranged in a layout with a barrel and two end caps. Collision events are recorded and reconstructed if they pass three levels of trigger (hardware, online software, and offline filter), each using complementary information from the subdetectors.

B. Monte Carlo generators and simulation

Signal and background processes $e^+e^- \to X\gamma$ are simulated with the AFKQED event generator, which is based on QED for $e^+e^- \to \mu^+\mu^-\gamma$ and Ref. [23] for hadronic production. LO ISR and FSR emission is simulated for $e^+e^- \to \mu^+\mu^-\gamma$, while LO FSR is neglected for hadronic processes. The main photon (hereafter called the "ISR" photon) is emitted within the angular range $20° < \theta_\gamma^* < 160°$ in the e^+e^- c.m. system, bracketing the photon detection range with a margin for resolution. Additional ISR photons are generated with the structure function method [24], and additional FSR photons with the PHOTOS [25] program. Additional ISR photons are emitted along the e^+ or e^- beam particle direction. A minimum mass $m_{X\gamma_{\mathrm{ISR}}} > 8\,\mathrm{GeV}/c^2$ is imposed at generation, which puts an upper bound on the additional ISR photon energy. Samples corresponding to 5 to 10 times the data are generated for the signal $e^+e^- \to \mu^+\mu^-\gamma$ and $e^+e^- \to \pi^+\pi^-\gamma$ channels, as well as large samples of backgrounds from the other two-prong and multihadron ISR processes. Background processes $e^+e^- \to q\bar{q}$ ($q = u, d, s, c$) are generated with the JETSET [26] generator, and $e^+e^- \to \tau^+\tau^-$ with the KORALB [27] program. The response of the *BABAR* detector is simulated using the GEANT4 [28] package.

C. Event selection

Event selection follows the same procedure as the selection of two-charged particle ISR events used for cross section measurements [6]. It requires a photon with energy $E_\gamma^* > 3\,\mathrm{GeV}$ in the e^+e^- c.m. and laboratory polar angle with respect to the e^- beam in the range [0.35–2.4] rad, and exactly two tracks of opposite charge, each with momentum $p > 1\,\mathrm{GeV}/c$ and within the angular range [0.40–2.45] rad. If more than one photon is detected, the candidate with the highest E_γ^* is taken to be the "ISR" photon. To ensure a rough momentum balance at an early stage of the selection, the "ISR" photon is required to lie within 0.3 rad of the missing momentum of the charged particles (or of the tracks plus the other photons). The tracks are required to have at least 15 hits in the DCH, to originate within 5 mm of the collision axis and within 6 cm from the beam spot along the beam direction, and to extrapolate to the DIRC and IFR active areas in order to exclude low-efficiency regions. Both tracks are required to be identified either as

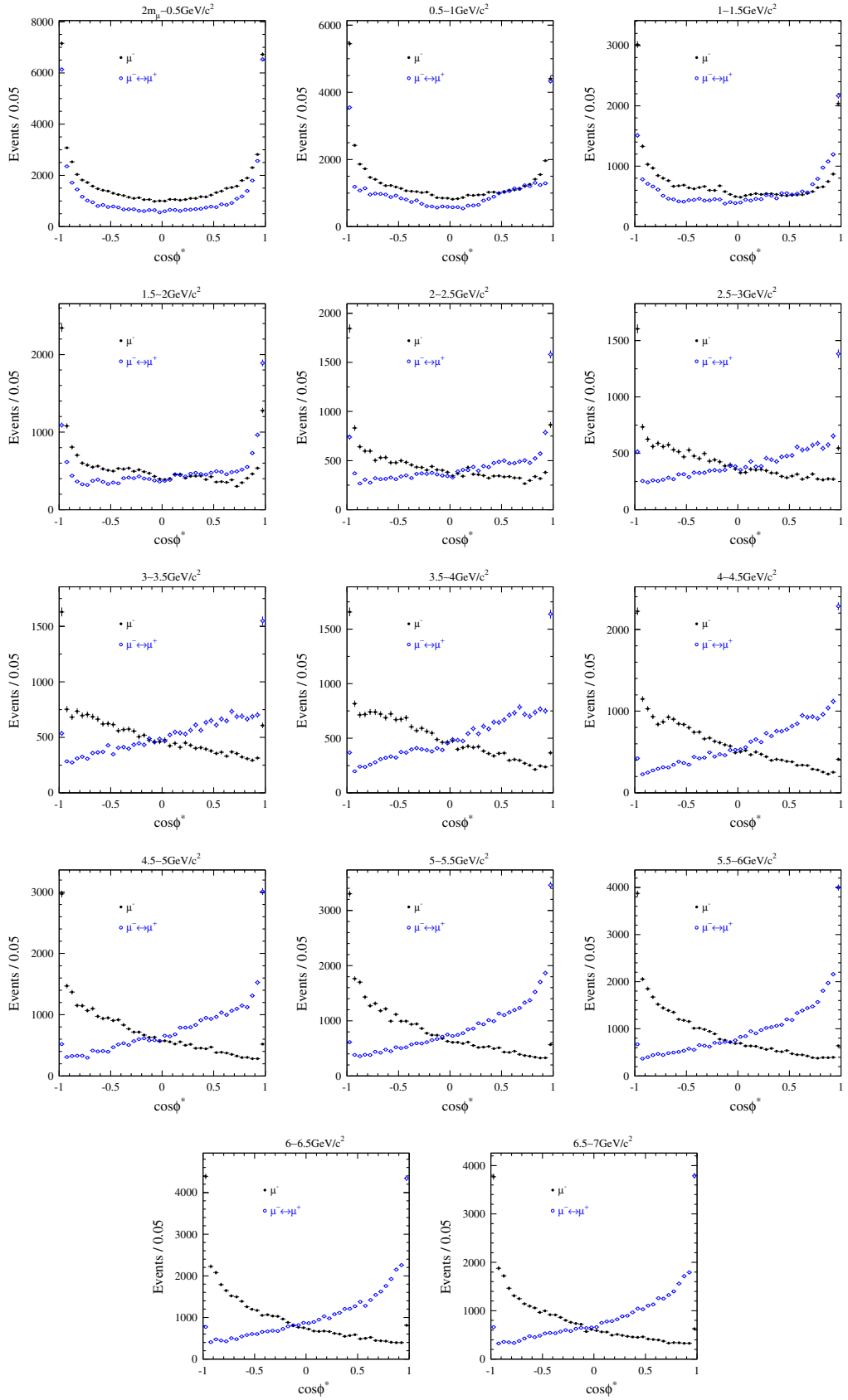

FIG. 6 (color online). The $\cos\phi^*$ distributions for $e^+e^- \to \mu^+\mu^-\gamma$ data in $0.5\,\mathrm{GeV}/c^2$ $m_{\mu\mu}$ intervals. The points labeled "μ^-" refer to the configurations with $\phi^*_- \in [0,\pi]$, while the points labeled "$\mu^- \leftrightarrow \mu^+$" correspond to $\phi^*_+ \in [0,\pi]$.

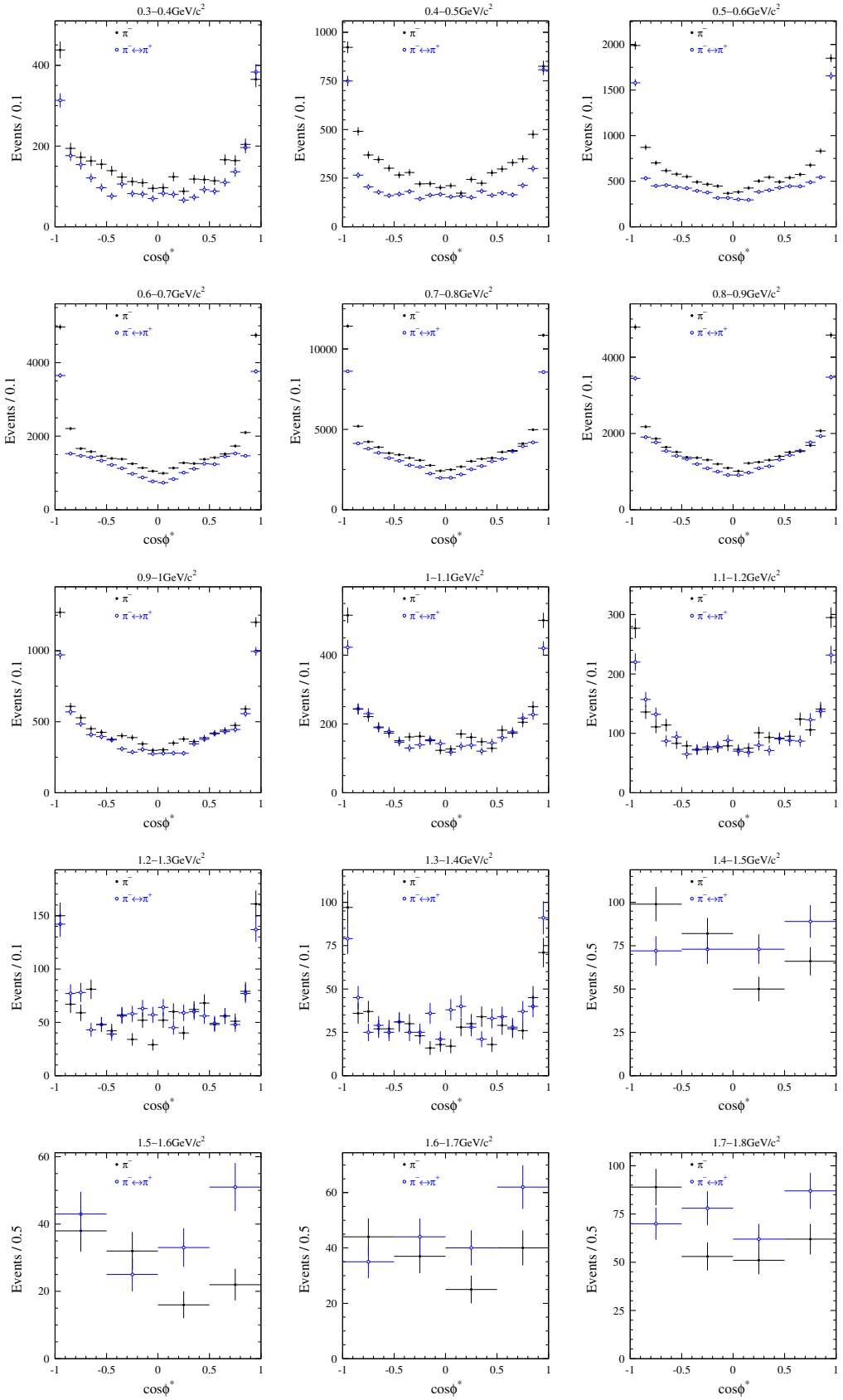

FIG. 7 (color online). The $\cos\phi^*$ distributions for $e^+e^- \to \pi^+\pi^-\gamma$ data in 0.1 GeV/c^2 $m_{\pi\pi}$ intervals. The points labeled "π^-" refer to the configurations with $\phi^*_- \in [0,\pi]$, while the points labeled "$\pi^- \leftrightarrow \pi^+$" correspond to $\phi^*_+ \in [0,\pi]$.

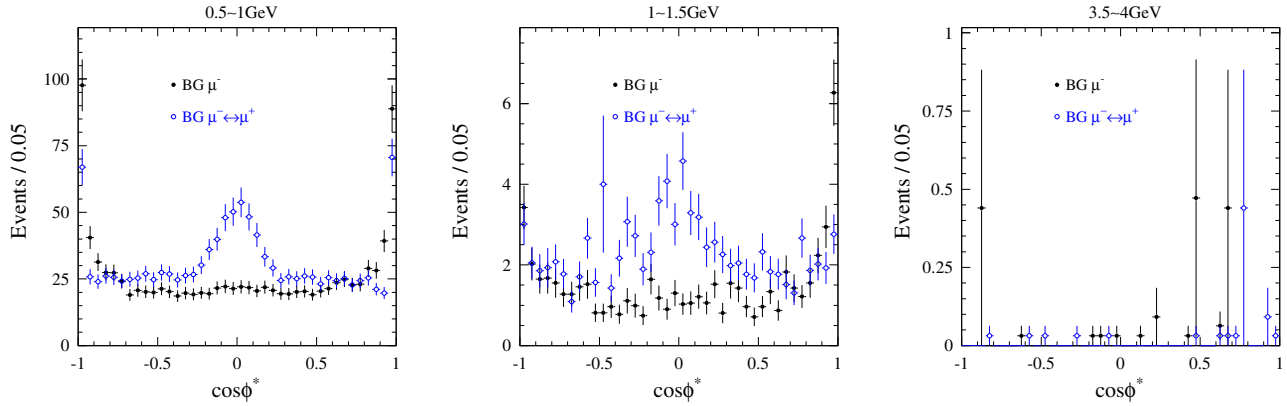

FIG. 8 (color online). Backgrounds estimated with MC for $e^+e^- \to \mu^+\mu^-\gamma$ as a function of $\cos\phi^*$ in selected $m_{\mu\mu}$ intervals. The points labeled "μ^-" refer to the configurations with $\phi^*_- \in [0,\pi]$, while the points labeled "$\mu^- \leftrightarrow \mu^+$" correspond to $\phi^*_+ \in [0,\pi]$.

muons or as pions. To suppress the background to $\pi^+\pi^-\gamma$ at threshold due to the $e^+e^- \to \gamma\gamma$ process followed by a photon conversion and misidentification of both electrons as pions, it is further required that the distance in the transverse plane V_{xy} between the vertex of the two tracks and the beam collision point be less than 0.5 cm for $m_{\pi\pi} < 0.5\,\mathrm{GeV}/c^2$. Electron background to $\mu^+\mu^-\gamma$ is negligible over the full mass range.

In order to suppress multihadron ISR events and reduce higher-order radiative processes, the selected two-prong candidates are subjected to a one-constraint kinematic fit to the $e^+e^- \to x^+x^-\gamma$ hypothesis ($x = \mu, \pi$), in which only the two good charged-particle tracks are taken as input and the corresponding missing mass is constrained to the null photon mass. The χ^2 value of the kinematic fit is required to be less than 15.

D. Charge asymmetry calculation

For a complete topology of the final states, the azimuth ϕ^* defined in Sec. II B should cover the 2π range. However, the event sample with x^- azimuth $\phi^*_- \in [0,\pi]$ is complementary to the sample with x^+ azimuth $\phi^*_+ \in [0,\pi]$, since $\phi^*_+ = \pi + \phi^*_-(\mathrm{mod}\,2\pi)$ in every event. This allows us to restrict ϕ^* to the range $[0,\pi]$ with no loss of phase space. After integrating over θ^*_γ and θ^*, the total event sample in a fixed m_{xx} interval subdivides into two subsamples: one with $\phi^*_- \in [0,\pi]$ (N_-), and the other with $\phi^*_+ \in [0,\pi]$ (N_+).

We obtain separately the distributions in $\cos\phi^*$ of the $N^{\mathrm{obs}}_\pm$ samples in data, namely $N^{\mathrm{obs}}_-(\cos\phi^*)$ with $\phi^*_- = \phi^*$ and $N^{\mathrm{obs}}_+(\cos\phi^*)$ with $\phi^*_+ = \phi^*$. Distributions of background events $N^{\mathrm{BG}}_\pm(\cos\phi^*)$ are determined separately for each subsample, as described below. Likewise, efficiencies are split into $\epsilon_\pm(\cos\phi^*)$ and computed using the full simulation of $e^+e^- \to x^+x^-\gamma$ ($x = \mu, \pi$) events, with corrections for the differences between data and simulation (see Secs. VI C and VII C). In a given $m_{\mu\mu}$ ($m_{\pi\pi}$) interval, the asymmetry at a given $\cos\phi^*$ is derived from the difference between the $N_-(\cos\phi^*)$ and $N_+(\cos\phi^*)$ yields, corrected for efficiency, and is obtained from the following expression:

$$A(\cos\phi^*) = \frac{N_-(\cos\phi^*)/\epsilon_-(\cos\phi^*) - N_+(\cos\phi^*)/\epsilon_+(\cos\phi^*)}{N_-(\cos\phi^*)/\epsilon_-(\cos\phi^*) + N_+(\cos\phi^*)/\epsilon_+(\cos\phi^*)}, \tag{13}$$

where $N_\pm(\cos\phi^*) = N^{\mathrm{obs}}_\pm(\cos\phi^*) - N^{\mathrm{BG}}_\pm(\cos\phi^*)$.

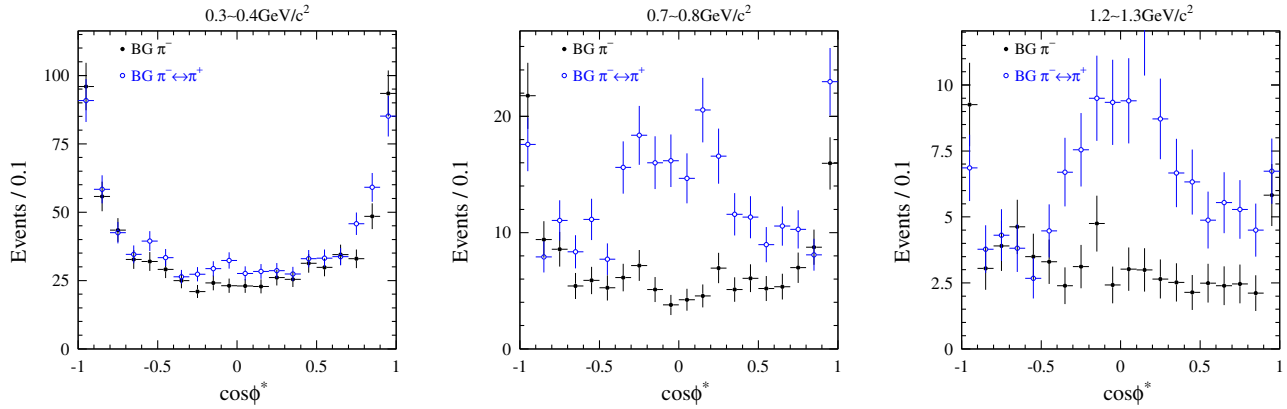

FIG. 9 (color online). Backgrounds estimated with MC for $e^+e^- \to \pi^+\pi^-\gamma$ as a function of $\cos\phi^*$ in selected $m_{\pi\pi}$ intervals. The points labeled "π^-" refer to the configurations with $\phi^*_- \in [0,\pi]$, while the points labeled "$\pi^- \leftrightarrow \pi^+$" correspond to $\phi^*_+ \in [0,\pi]$.

Note that distributions of $N_{\pm}(\cos\phi^*)$ can be obtained in each $(m_{xx}, \theta^*_\gamma, \cos\theta^*)$ cell of the phase space, and the asymmetry defined by Eq. (13) can be calculated. However, this one-dimensional quantity $A(\cos\phi^*)$ is a valid definition of charge asymmetry only when the variable $\cos\theta^*$ is integrated within a symmetric range. This is a consequence of the fact that the $x^+ \leftrightarrow x^-$ interchange means both $\phi^* \to \pi + \phi^*$ and $\cos\theta^* \to -\cos\theta^*$, and therefore a non-null value of $A(\cos\phi^*)$ in an arbitrary $\cos\theta^*$ interval is not an intrinsic signature of ISR-FSR interference.

E. Event samples and backgrounds after selection

The $\cos\phi^*$ distributions $N^{\rm obs}_{\pm}(\cos\phi^*)$ for $e^+e^- \to \mu^+\mu^-\gamma$ obtained in data after the overall event selection are shown in Fig. 6, for $\mu\mu$ mass intervals ranging from threshold to 7 GeV/c^2. The event distributions $N^{\rm obs}_{\pm}(\cos\phi^*)$ obtained for $e^+e^- \to \pi^+\pi^-\gamma$ in data are shown in Fig. 7, in 0.1 GeV/c^2 mass intervals ranging from 0.3 GeV/c^2 to 1.8 GeV/c^2.

The backgrounds remaining after selection are estimated using the full simulation, normalized to the data luminosity, of the nonsignal two-prong ISR events, multihadron events produced through ISR, $e^+e^- \to q\bar{q}$ events, and $\tau^+\tau^-$ events. The expected contamination for $e^+e^- \to \mu^+\mu^-\gamma$ as a function of $\cos\phi^*$ in typical $m_{\mu\mu}$ intervals is shown in Fig. 8, where the total error is the quadratic sum of the statistical error and 10% systematic uncertainty on normalization [6]. Likewise, the estimated backgrounds for $e^+e^- \to \pi^+\pi^-\gamma$ in typical $m_{\pi\pi}$ intervals are shown in Fig. 9.

V. ACCEPTANCE AND DETECTOR EFFICIENCY EFFECTS ON THE CHARGE ASYMMETRY

The charge asymmetry measurement is affected by the event reconstruction and selection. These experimental effects are investigated using the full simulation of signal events through changes of the raw charge asymmetry, defined as $A^{\rm raw} = (N_- - N_+)/(N_- + N_+)$, which are observed after each selection step as a function of $\cos\phi^*$.

A. Study of the effects with the muon simulation

1. Kinematic acceptance

The kinematic acceptance includes the angular acceptance for the primary photon and the two charged-particle tracks, and the momentum restriction ($p > 1\,{\rm GeV}/c$) applied to charged-particle tracks. Each kinematic selection is found to modify the slope of the raw charge asymmetry significantly, though the total effect on the slope from the kinematic requirements altogether turns out to be small due to accidental cancellations.

It is worthwhile to note that the kinematic selection in itself is charge symmetric. Hence the observed bias on the measured raw charge asymmetry is a cross effect of physical charge-asymmetric kinematics and charge-symmetric detector acceptance. It does vanish for a null physical charge asymmetry. As checked with a $\mu^+\mu^-\gamma$ simulated sample produced by ISR only, no fake charge asymmetry emerges from the kinematic selection.

2. Software trigger and tracking

Biases on the raw charge asymmetry measurement originate from the software trigger and the track reconstruction. They are observed in the low-mass region, as illustrated in Fig. 10 and vanish at high mass ($m_{\mu\mu} > 1.5\,{\rm GeV}/c^2$).

The common origin of the mass-dependent trigger and tracking inefficiencies is geometrical and has been thoroughly studied for the $\pi^+\pi^-$ cross-section measurement [6]. Converging trajectories in the DCH of oppositely deflected tracks emitted in close-by directions confuses the track reconstruction and causes both the software trigger and the final tracking inefficiencies. In the charge-conjugate configuration, in which the positive and negative tracks are interchanged, tracks diverge in the magnetic field and are well separated in the transverse plane, although with the same absolute azimuthal opening angle. The efficiencies are consequently charge asymmetric, sharply reduced for

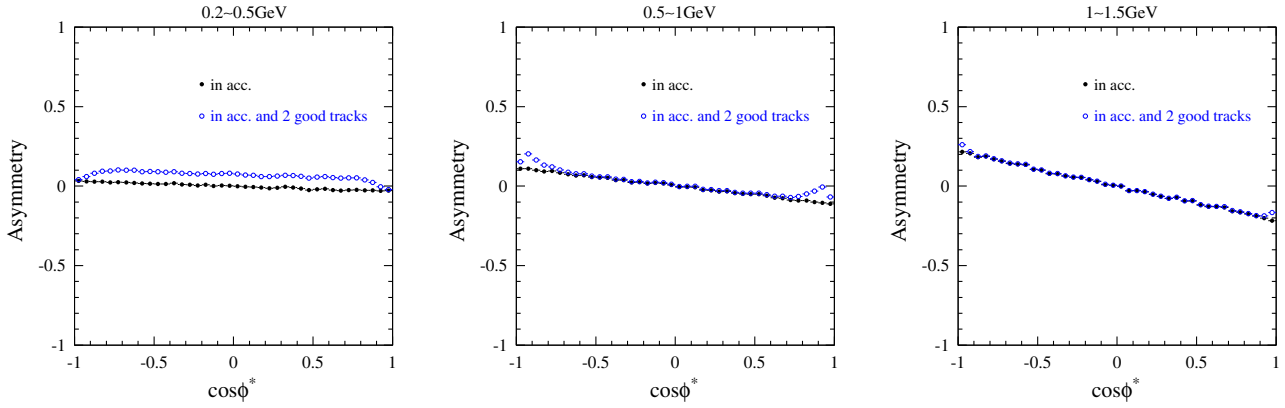

FIG. 10 (color online). Raw charge asymmetry as a function of $\cos\phi^*$ in selected $m_{\mu\mu}$ intervals, for $e^+e^- \to \mu^+\mu^-\gamma$ MC events with (◦) and without (•) reconstruction of two good charged-particle tracks, where the events are already required to be within the kinematic acceptance.

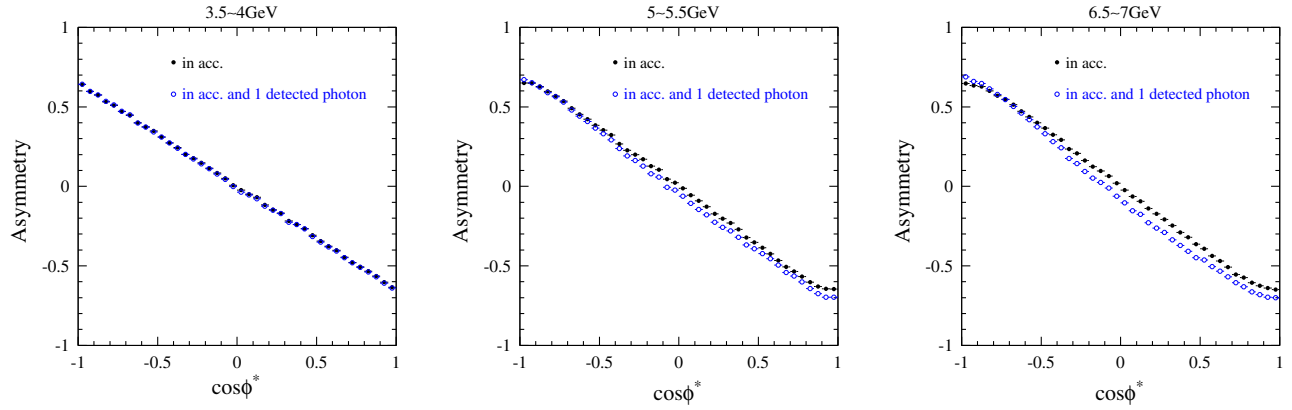

FIG. 11 (color online). Raw charge asymmetry as a function of $\cos\phi^*$ in selected $m_{\mu\mu}$ intervals, for $e^+e^- \to \mu^+\mu^-\gamma$ MC events with (◦) and without (•) the requirement of the reconstruction of the "ISR" photon, where the events are already required to be within the kinematic acceptance.

overlapping tracks in low-$m_{\mu\mu}$ regions, at $\Delta\phi$ values close to zero but always positive, where $\Delta\phi$ is the signed angular difference between the azimuths of the positive and negative tracks

$$\Delta\phi = (\phi_+ - \phi_-) \in [-\pi, \pi]. \tag{14}$$

3. "ISR" photon reconstruction

The event selection requires that an "ISR" photon with $E^*_\gamma > 3\,\mathrm{GeV}$ be measured in the EMC. The raw charge asymmetries for the fully simulated events with and without the requirement of the "ISR" photon being reconstructed are shown in Fig. 11, where the events are already required to be within the kinematic acceptance. Effects are observed in high-$m_{\mu\mu}$ regions.

The origin of a charge-asymmetric photon reconstruction inefficiency is again geometrical. In case one of the charged-particle tracks and the "ISR" photon overlap in the EMC, the shower produced by the "ISR" photon is mistakenly associated to the charged-particle track, and the "ISR" photon is lost. In the charge-conjugate configuration, no overlap occurs because of the opposite deflection of the charged-particle track in the magnetic field. The overlap happens at $\Delta\phi = -\pi + \varepsilon$ where ε is a small positive quantity, and as a consequence, the "ISR" photon reconstruction efficiency is charge asymmetric, strongly reduced around $\Delta\phi \sim -\pi$. As the overlap of one charged-particle track and the "ISR" photon occurs preferentially at high mass, due to phase space, the corresponding effects are only observed at $m_{\mu\mu} > 3.5\,\mathrm{GeV}/c^2$.

4. Muon identification

The charge asymmetry measurement is also affected by muon identification, in the low- and high-$m_{\mu\mu}$ regions, as shown in Fig. 12. Charge-asymmetric inefficiency of muon identification results again from event topologies. The first cause, which affects low-$m_{\mu\mu}$ regions, is the overlap of the two charged-particle tracks at the IFR, which confuses the muon identification algorithm. The second cause is the partial overlap of one charged-particle track and the "ISR" photon at the EMC, which makes the track look unlike a muon. The latter effect is more pronounced at high mass, when a muon and the "ISR" photon are emitted in close-by directions. The efficiency of muon identification as a function of $\Delta\phi$ exhibits a sharp dip at positive $\Delta\phi$ at low mass, and at $\Delta\phi \simeq -\pi$ at high mass.

5. Summary of the acceptance and detector efficiency effects in the $\mu^+\mu^-\gamma$ process

The overall efficiencies $\epsilon_\pm$ needed to correct the $N_\pm$ event yields entering the charge asymmetry measurement [Eq. (13)] are the overall result of the acceptance-induced and detector asymmetries discussed above. They are determined using the full simulation, separately for the $N_\pm$ samples.

As previously discussed, the detector inefficiencies are mostly caused by the spatial overlap of trajectories occurring in the detector: two-track overlaps in the DCH and the IFR, respectively for $\Delta\phi = 0.1 \pm 0.1$ and 0.5 ± 0.2 and affecting masses below $2\,\mathrm{GeV}/c^2$, and the photon-muon overlap in the EMC, for $\Delta\phi \gtrsim -\pi$ and affecting masses above $4\,\mathrm{GeV}/c^2$. These various overlap effects contribute very asymmetrically to the two $N_\pm$ samples, due to a complete correlation between the $\cos\phi^*_\pm$ and $\Delta\phi$ variables. This is demonstrated in Fig. 13, which shows that the N_+ (N_-) sample corresponds to $\Delta\phi > 0$ ($\Delta\phi < 0$). Since the two-track overlaps occur for $\Delta\phi > 0$, one expects $\epsilon_- > \epsilon_+$. For the photon-muon overlap with nearly opposite tracks the situation is reversed.

As a consequence, as summarized in Fig. 14 (Sec. VI), the acceptance and detector inefficiencies induce a change ΔA in the observed charge asymmetry magnitude and also distort the linear dependence on $\cos\phi^*$. The dominant effects are from geometric acceptance, "ISR" photon reconstruction and the track momentum requirement $p > 1\,\mathrm{GeV}/c$.

However, although the detector is not completely charge symmetric, Fig. 13 shows that the effects producing

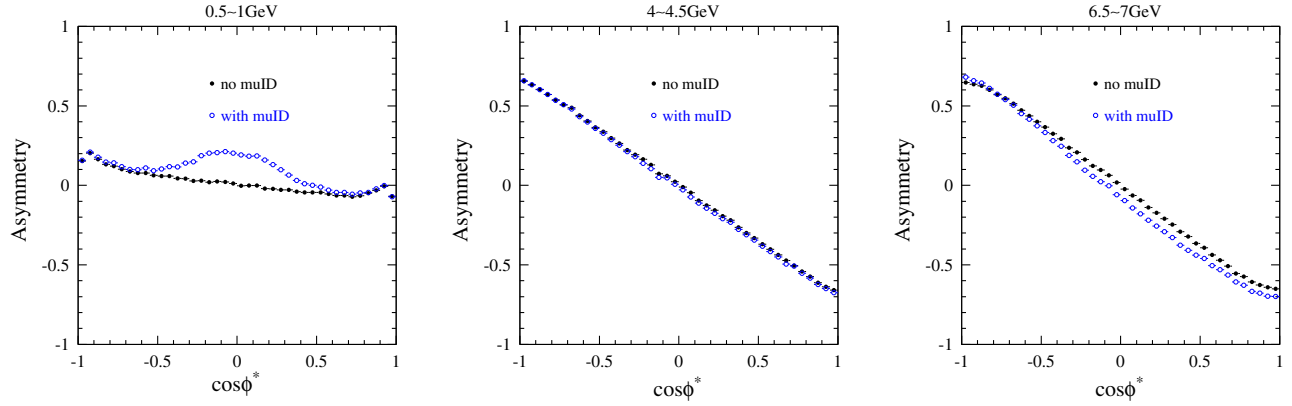

FIG. 12 (color online). Raw charge asymmetry as a function of $\cos\phi^*$ in selected $m_{\mu\mu}$ intervals, for $e^+e^- \to \mu^+\mu^-\gamma$ MC events with (◦) and without (•) the two-muon identification, where the events are already required to be within the kinematic acceptance and have two good charged-particle tracks reconstructed.

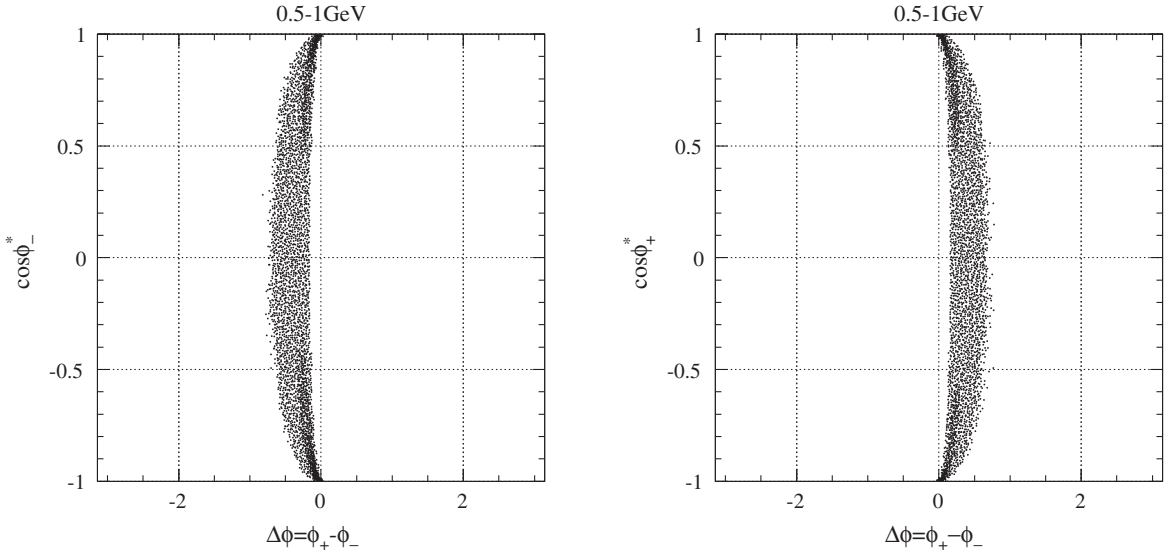

FIG. 13. (Left) Distribution of $\cos\phi^*_-$ vs $\Delta\phi$ for the N_- sample ($\phi^*_- \in [0,\pi]$) in the (0.5–1.0) GeV/c^2 mass interval for the $\mu^+\mu^-\gamma$ MC. (Right) The same for the N_+ sample ($\phi^*_+ \in [0,\pi]$).

an asymmetry are nearly symmetric in $\cos\phi^*$. The A_0 observable introduced in Eq. (5) is thus expected to be robust against such effects. Overall, the slope of the asymmetry is barely affected by detector inefficiencies and event selection. In the $\mu^+\mu^-\gamma$ process, the maximum effects, of a few 10^{-2}, take place around $m_{\mu\mu} \sim 2$–$4\,\mathrm{GeV}/c^2$. In the low-mass region $[0.5$–$1.0]\,\mathrm{GeV}/c^2$, the effect from the overall selection is at the level of a few 10^{-3}.

B. Study of the effects with the pion simulation

The acceptance and detector effects are also studied with the simulated $e^+e^- \to \pi^+\pi^-\gamma$ events. The overall effect around the ρ resonance ($m_{\pi\pi} \in [0.4, 1.2]\,\mathrm{GeV}/c^2$) is $(0.30 \pm 0.07) \times 10^{-2}$ on average.

As the charge asymmetry is null for $e^+e^- \to \pi^+\pi^-\gamma$ MC events, generated with no LO FSR, the acceptance effects on the slope of the charge asymmetry are quite small for any selection requirement, including the kinematic ones. This is in contrast with the $\mu^+\mu^-\gamma$ case, where the individual kinematic requirements induce large effects. However this conclusion holds only if the charge asymmetry in the data is actually null. If a sizable asymmetry is measured, the bias introduced by the cross effect of acceptance and asymmetry has to be evaluated and corrected (Sec. VII B).

VI. RESULTS ON THE CHARGE ASYMMETRY IN THE $e^+e^- \to \mu^+\mu^-\gamma$ PROCESS

The measured raw charge asymmetry after the complete event selection for the data is obtained as a function of $\cos\phi^*$ in various $m_{\mu\mu}$ intervals, and shown in Fig. 14. It is consistent to the first order with the full simulation of $e^+e^- \to \mu^+\mu^-\gamma$ events, except in the mass interval populated by the J/ψ resonance (3.0–3.5 GeV/c^2).

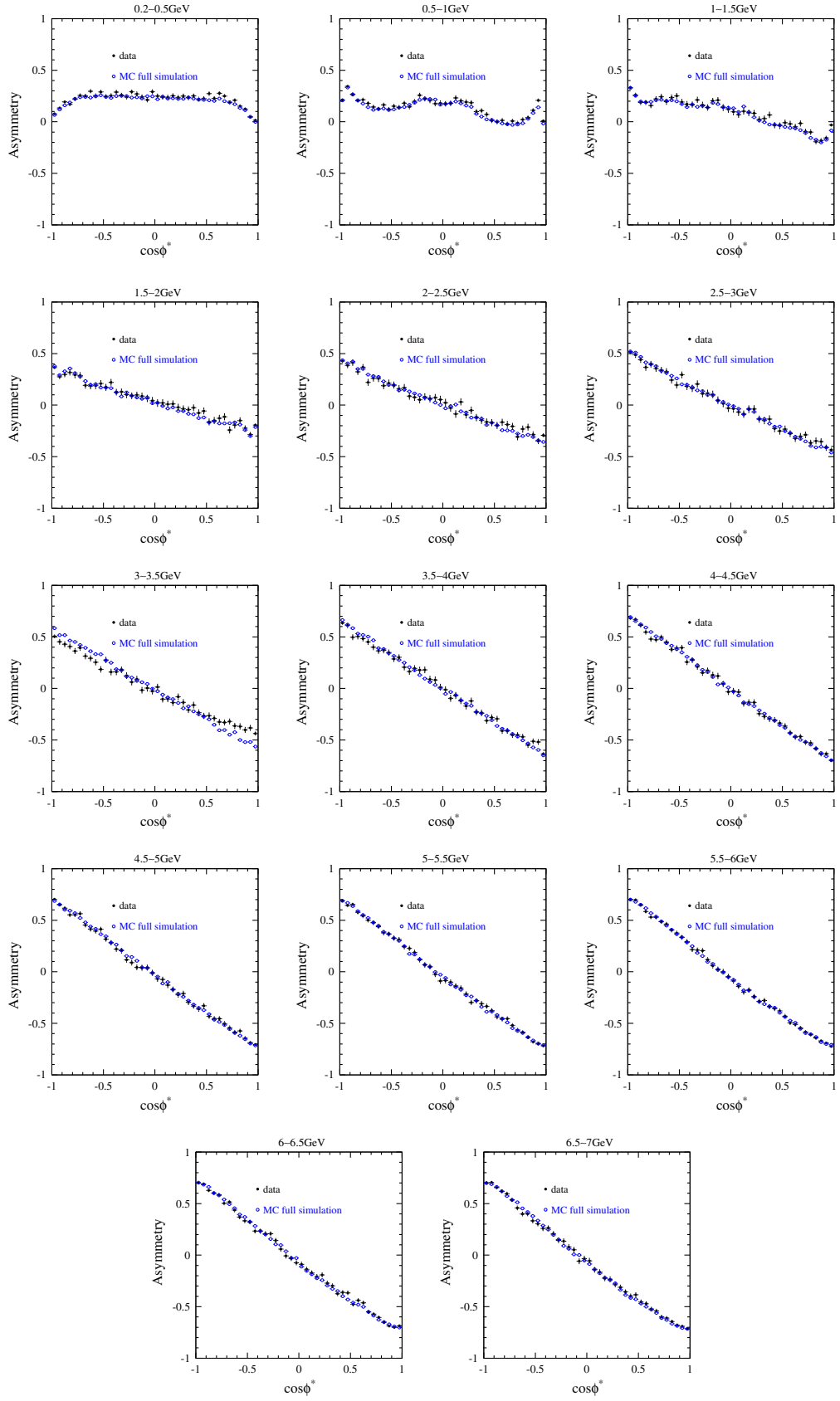

FIG. 14 (color online). Raw charge asymmetry as a function of cos ϕ^* for $\mu^+\mu^-\gamma$ events in data (•) and MC (○), in various $m_{\mu\mu}$ intervals, after the complete event selection.

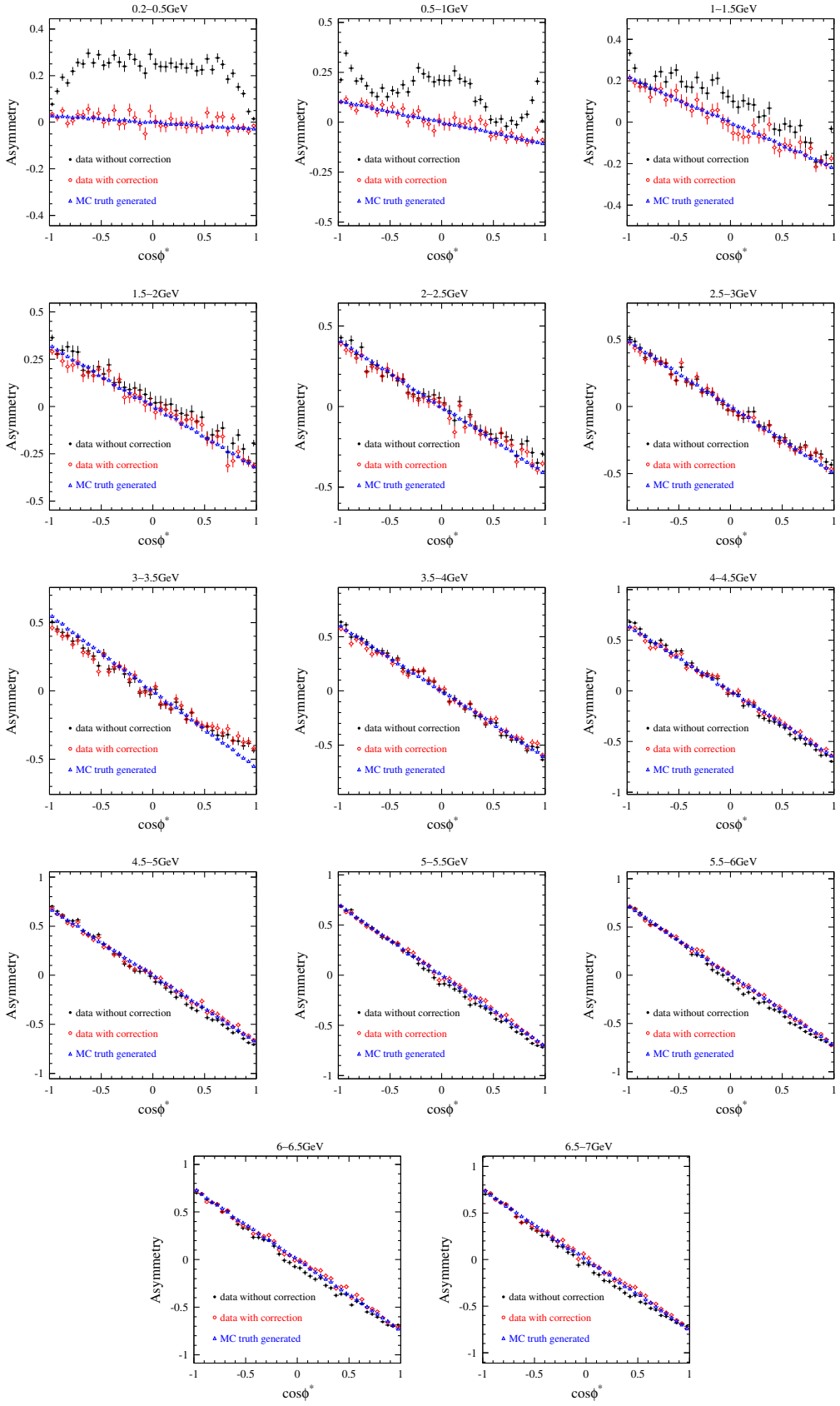

FIG. 15 (color online). Charge asymmetry in $e^+e^- \to \mu^+\mu^-\gamma$ data before (•) and after (○) background subtraction and efficiency corrections, and for MC (Δ) at generation level.

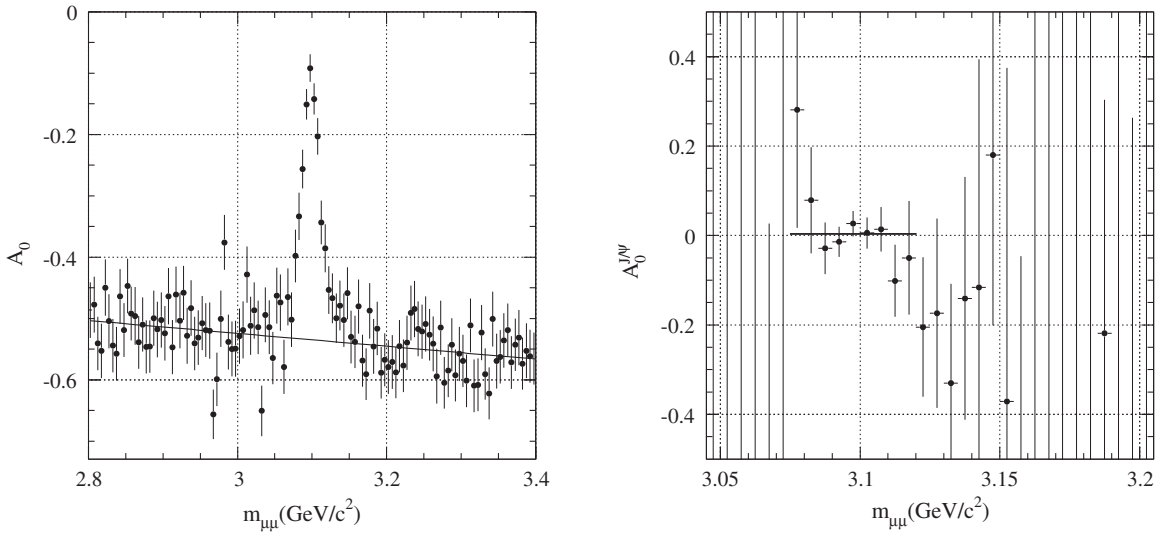

FIG. 16. (Left) The measured charge asymmetry as a function of $\mu\mu$ mass near the J/ψ resonance. (Right) The derived charge asymmetry for $\mu^+\mu^-\gamma$ from $e^+e^- \to \gamma J/\psi$.

This is expected as J/ψ production is not considered in AFKQED.

The physical charge asymmetry for $e^+e^- \to \mu^+\mu^-\gamma$ is obtained from the measured $\cos\phi^*$ distributions after background subtraction and efficiency correction. The background dependence on $\cos\phi^*$ is estimated with the simulation for each of the samples $\phi^*_\pm = \phi^* \in [0, \pi]$, as explained above. Similarly, the overall efficiency $\epsilon_\pm$ is obtained with fully simulated $e^+e^- \to \mu^+\mu^-\gamma$ events, and corrected for data/MC differences in detector response. The efficiency differences between data and simulation have been studied extensively for the cross-section measurements of $e^+e^- \to \mu^+\mu^-\gamma$ and $e^+e^- \to \pi^+\pi^-\gamma$ [6]. They are parametrized as a function of the azimuthal opening angle $\Delta\phi$ between the two muons, and projected onto the $\cos\phi^*$ variable by sampling with MC.

The charge asymmetry distributions for $e^+e^- \to \mu^+\mu^-\gamma$ data after background subtraction and efficiency correction, as well as the charge asymmetry for $e^+e^- \to \mu^+\mu^-\gamma$ MC at generation level, are shown in Fig. 15. While the $\cos\phi^*$ dependence of the measured raw charge asymmetry is not linear, the corrected data distributions are quite consistent with the MC distributions at generation level. The slopes of charge asymmetry in various mass intervals are obtained by fitting the background-subtracted efficiency-corrected charge asymmetry distributions to $A_0 \cos\phi^*$.

A. Test of the charge asymmetry with $J/\psi \to \mu^+\mu^-$ events in data

Since $e^+e^- \to \gamma J/\psi$ with on-shell $J/\psi \to \mu^+\mu^-$ is a pure ISR process at $\Upsilon(4S)$ energies, the $J/\psi \to \mu^+\mu^-$ sample in the data provides a test of fake asymmetries that could arise in the analysis.

To overcome the limited statistics of the $J/\psi \to \mu^+\mu^-$ sample, a loosened event selection is applied, with the muon identification requirement removed, which provides a gain in statistics by a factor of about 4, with no significant increase of the hadronic background. The $m_{\mu\mu}$ spectrum shows a clear J/ψ peak, over a linear QED background. Defining $A_0^{J/\psi}$ and $A_0^{\rm QED}$, the respective slopes of the charge asymmetry for J/ψ and underlying QED events, the slope A_0 measured in the vicinity of the J/ψ resonance is the average

$$A_0 = \frac{A_0^{J/\psi} N_{J/\psi} + A_0^{\rm QED} N_{\rm QED}}{N_{J/\psi} + N_{\rm QED}}, \tag{15}$$

where $N_{J/\psi}$ and $N_{\rm QED}$ are the yields from J/ψ and QED, respectively. The quantities $N_{\rm QED}$ and $N_{J/\psi}$ are obtained by fitting the mass spectrum with a sum of a linear QED component and a Gaussian J/ψ signal, with fixed width equal to the mass resolution at the J/ψ and centered at the nominal J/ψ mass. The slope $A_0^{\rm QED}$ is obtained by fitting the charge asymmetry in the J/ψ sidebands. The measured slope of the charge asymmetry as a function of $m_{\mu\mu}$ is shown in Fig. 16: the expected behavior is clearly observed, with a smooth variation from the QED continuum with a large negative value and a sharp peak approaching a null slope on the J/ψ resonance. The specific $A_0^{J/\psi}$ slope is obtained as a function of $m_{\mu\mu}$ in Fig. 16 according to Eq. (15): its value is stable across the J/ψ peak and a fit to a constant between 3.07 and 3.12 GeV/c^2 yields

$$A_0^{J/\psi} = (0.3 \pm 1.6) \times 10^{-2}, \tag{16}$$

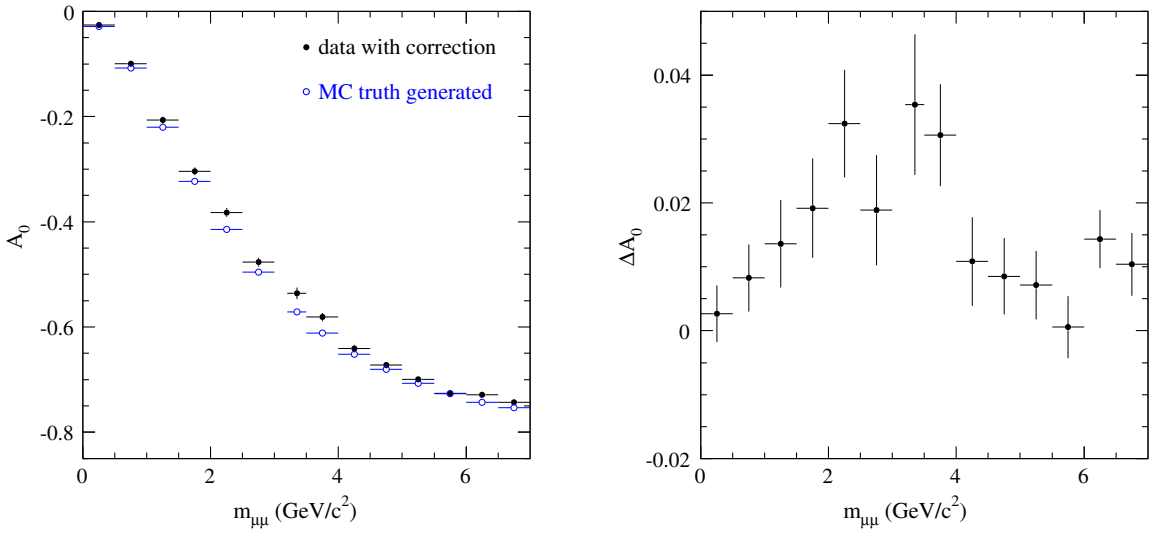

FIG. 17 (color online). The slope A_0 of charge asymmetry as a function of $m_{\mu\mu}$ in $e^+e^- \to \mu^+\mu^-\gamma$ data and in MC at generation level (left), and the absolute difference between them (right). The J/ψ mass region (3.0–3.2 GeV/c^2) is excluded. Only statistical uncertainties are shown.

which is consistent with zero, as expected from the ISR-only J/ψ production.

B. Comparison to QED

The final slope A_0 as a function of $m_{\mu\mu}$ measured on the data is shown in Fig. 17, together with the asymmetry at the MC generation level, and the difference between them. The mass interval containing the pure-ISR contribution from the J/ψ ($e^+e^- \to \gamma_{\rm ISR}J/\psi$, $J/\psi \to \mu^+\mu^-$), discussed in detail in Sec. VI A, is excluded. The absolute difference between data and MC $\Delta A_0 = A_0^{\rm data} - A_0^{\rm MC}$ is at a few percent level (0–3%).

The measured slope of charge asymmetry is negative throughout the mass range under study, and its magnitude increases with mass, reaching values as large as -0.7 at 5 GeV/c^2, in agreement with the trend predicted by QED. However, while data and LO QED agree within 10^{-2} at mass less than 1 GeV/c^2 and above 5 GeV/c^2, a small but significant discrepancy shows up for intermediate mass, reaching $\sim 3 \times 10^{-2}$ between 1.5 and 4 GeV/c^2. Investigations of systematic uncertainties, both at the experimental and theoretical levels, are reported in the next section.

Due to the asymmetry of the beam energies at PEP-II, independent charge asymmetry measurements in two different kinematic regimes are provided by splitting the data into a forward ($\cos\theta^*_\gamma > 0$) sample and a backward ($\cos\theta^*_\gamma < 0$) sample. The full analysis, including background subtraction and efficiency correction, is redone on each sample separately. The results are shown in Fig. 18. A significant discrepancy between data and AFKQED is observed in the forward region, in the 1.5–4 GeV/c^2 mass region, while in the backward hemisphere data and AFKQED are consistent. The differences are quantified in Table I. No significant forward-backward difference is expected from the generator.

C. Systematic uncertainties

1. Experimental systematic effects

The primary sources of systematic uncertainty are the background estimation, data/MC differences in detector

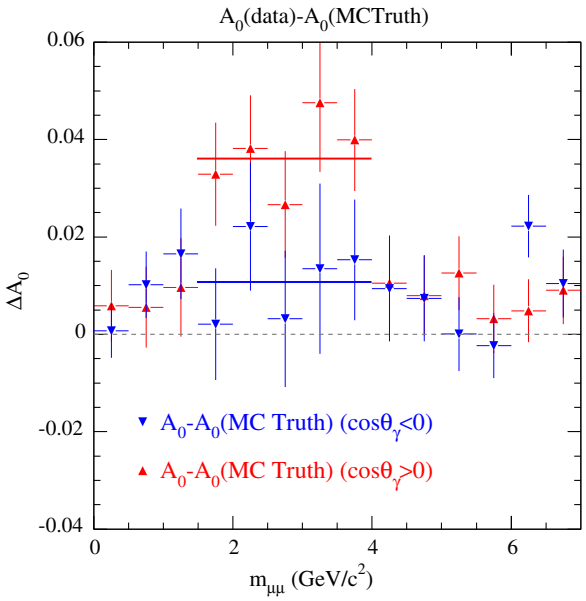

FIG. 18 (color online). The difference between the measured asymmetry slope in the $\mu^+\mu^-\gamma$ process and the AFKQED prediction, as a function of $m_{\mu\mu}$, excluding the J/ψ 3.0–3.2 GeV/c^2 region. Forward ($\cos\theta^*_\gamma > 0$) and backward ($\cos\theta^*_\gamma < 0$) hemispheres are analyzed separately. Statistical uncertainties only.

TABLE I. The difference (in 10^{-2} units) between the measured A_0 and the AFKQED prediction for the two mass intervals 1.5–4 and 4–7 GeV/c^2 in different $\cos\theta^*_\gamma$ regions. The last line gives the difference between the two regions $\cos\theta^*_\gamma > 0$ and $\cos\theta^*_\gamma < 0$. Statistical uncertainties only.

(10^{-2})	$1.5 < m_{\mu\mu} < 4\,\mathrm{GeV}/c^2$	$4 < m_{\mu\mu} < 7\,\mathrm{GeV}/c^2$
all $\cos\theta^*_\gamma$	2.65 ± 0.38	0.86 ± 0.22
$\cos\theta^*_\gamma > 0$	3.61 ± 0.50	0.76 ± 0.30
$\cos\theta^*_\gamma < 0$	1.08 ± 0.60	0.82 ± 0.31
difference	2.50 ± 0.78	-0.05 ± 0.42

response, and differences between the physical charge asymmetry in the data and in the generated MC events.

The difference ΔA_0 between the results with and without background subtraction is found to be well below 10^{-3} except in the 0.5–1.0 GeV/c^2 range, where it reaches 2×10^{-3} because of the larger ρ background with two pions misidentified as muons. Since the background level is known with better than 10% accuracy [6], the corresponding systematic uncertainty on the asymmetry slope is at most 2×10^{-4} throughout the studied mass range.

The trigger, tracking and μ-ID induce charge-asymmetric data/MC corrections, as overlap effects are not perfectly reproduced by simulation. However, the data/MC corrections have small effects on the charge asymmetry slope, at most 3×10^{-3}. Since the corrections have been measured with a precision of 10% or better [6], the corresponding systematic uncertainty on the asymmetry slope is less than 3×10^{-4}.

As explained in Sec. V A 1, the effects from the kinematic acceptance on the measured slope of the charge asymmetry depend on the physical charge asymmetry itself. The possible bias on the acceptance correction, induced by the physical charge asymmetry in the generator inaccurately reproducing the data, is studied using a sample of reweighted $e^+e^- \to \mu^+\mu^-\gamma$ MC events where weights are adjusted to yield the same asymmetry as measured in the data in each ($m_{\mu\mu}$, θ^*_γ, θ^*, $\cos\phi^*$) phase-space cell. The expected bias in the measurement from a difference of charge asymmetry between data and MC is found to be less than 5×10^{-3}, which is taken as a systematic uncertainty on the A_0 measurement.

2. Effects from imperfect simulation

Since a simple linear fit $A(\cos\phi^*) = A_0 \cos\phi^*$ might be questionable, we perform an alternate two-parameter fit on the charge asymmetry after efficiency corrections $A(\cos\phi^*) = A_0 \cos\phi^* + B_0$. The B_0 values obtained in data are a few 10^{-3} at most, while the asymmetry slopes A_0 deviate from the final values, which use the one-parameter fit, by less than 10^{-4}.

To investigate whether the observed discrepancy results from the efficiency corrections, we study the difference $\Delta A^{\mathrm{raw}}(\cos\phi^*)$ between the raw asymmetries observed in data and MC after full event selection. Although the raw asymmetry itself is not linear, especially at low mass (Fig. 14), the difference $\Delta A^{\mathrm{raw}}(\cos\phi^*)$ in each mass interval is observed to be linear with $\cos\phi^*$. In particular, there are no edge effects in the vicinity of $|\cos\phi^*| \simeq 1$, which could have resulted from different resolutions in data and MC. The results of the fits are shown in Fig. 19 (black points). The values of the slope of ΔA^{raw} are insensitive to whether the linear fit is a one-parameter or a two-parameter fit. The data-MC discrepancy in the 1.5–4 GeV/c^2 mass

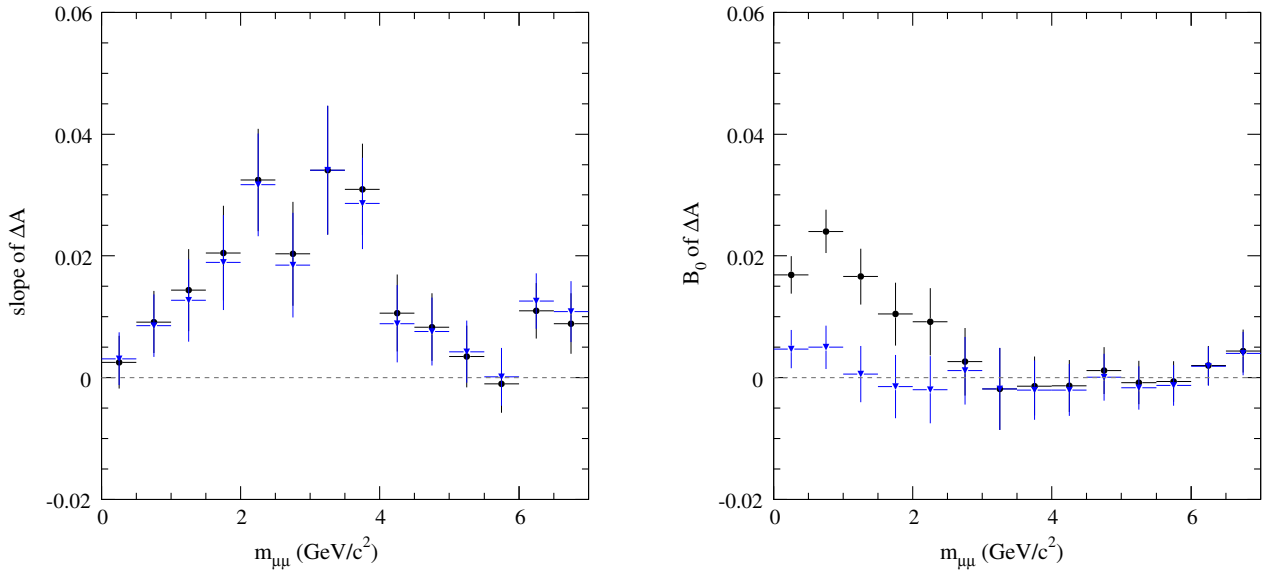

FIG. 19 (color online). (Left) Slope of the difference $\Delta A^{\mathrm{raw}}(\cos\phi^*)$ for $\mu^+\mu^-\gamma$ between the raw asymmetries observed in data and in MC before (black points) and after (blue triangles) the data/MC corrections, as a function of $m_{\mu\mu}$. (Right) Constant term of the two-parameter linear fits of $\Delta A^{\mathrm{raw}}(\cos\phi^*)$. Statistical uncertainties only.

region is already observed at the raw level, which excludes efficiency or resolution bias. The B_0 values returned by the two-parameter fit over $\Delta A^{\rm raw}$ depart from zero by up to 2.5×10^{-2} at low mass, as expected from imperfect detector simulation. When data/MC corrections of detector efficiencies are applied to the simulated raw data, the results are shown in Fig. 19 (blue triangles). The B_0 values are reduced to a few 10^{-3}, while the slope of $\Delta A^{\rm raw}$ is not changed by more than 3×10^{-3}.

When performed on the forward and backward samples independently, the study at the raw data level confirms that the data-MC discrepancy in the 1.5–4 GeV/c^2 mass interval is confined to the forward region, where the slope of $\Delta A^{\rm raw}$ is significantly non-null by $\sim 5\sigma_{\rm stat}$ while it is consistent with zero within $2\sigma_{\rm stat}$ over the full mass range for the $\cos\theta^*_\gamma < 0$ sample. In contrast, the fitted B_0 values are consistent with each other in the two samples, except at very low mass ($m_{\mu\mu} < 1\,{\rm GeV}/c^2$).

Comparisons of the data and MC distributions of event variables entering the asymmetry analysis are performed, in particular near the acceptance boundaries. A sizable departure is observed in the high-E_γ, low-θ_γ region, in the forward $\cos\theta^*_\gamma > 0$ hemisphere. However, the asymmetry measurement is found to be insensitive to this discrepancy at very forward photon angles. To investigate whether different resolutions in data and MC might bias the efficiency corrections and the event assignment to the N_+ or N_- samples, the analysis is fully redone with tighter acceptance requirements. The change of asymmetry slope is small, $(4 \pm 3) \times 10^{-3}$. Conservatively, a systematic uncertainty of 7×10^{-3} is assigned to account for imperfect simulation near the edges of the selected phase space.

The studies above first show that, although acceptance and detector inefficiency effects are important, they are well accounted for in the simulation. Data/MC corrections are found to significantly reduce the symmetric component of the asymmetry (B_0), but most importantly, the studies demonstrate that the measurement of the asymmetry slope is robust against uncertainties in the efficiency corrections.

As a global test to differentiate between an uncorrected experimental bias and a true deviation from the QED prediction, the difference between the measured asymmetry and the theoretical one, as implemented in AFKQED, is studied as a function of $\cos\phi^*$ for the events in the mass interval 1.5–4 GeV/c^2 where the deviation is the largest (excluding the J/ψ3.0–3.2 GeV/c^2 region). As shown in Fig. 20, a linear dependence is indeed observed. This supports the assertion that the deviation we observe does not originate from a detector effect unaccounted for in the simulation.

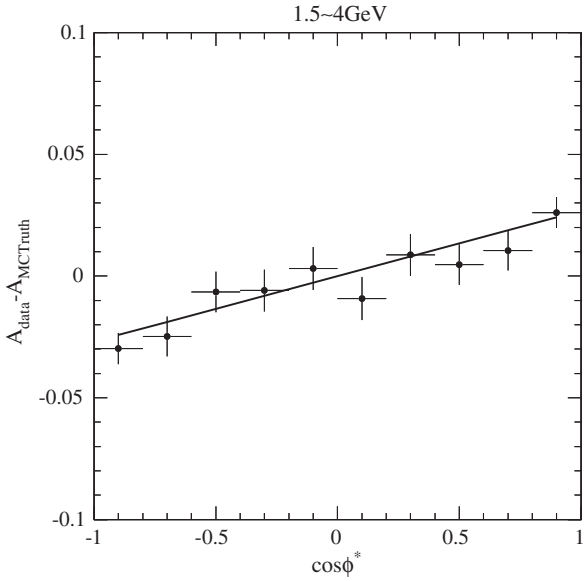

FIG. 20. The difference between the measured asymmetry in the $\mu^+\mu^-\gamma$ process and the QED prediction, as implemented in AFKQED, as a function of $\cos\phi^*$ for the events in the mass interval 1.5–4 GeV/c^2, excluding the J/ψ3.0–3.2 GeV/c^2 region. The result of a linear fit is shown by the solid line.

3. Theoretical systematic effects

The AFKQED event generator only includes the LO QED interference between ISR and FSR amplitudes. Additional photons generated independently for ISR and FSR, induce a change in asymmetry through kinematics. The NLO contributions to the QED interference are studied with the latest version of the PHOKHARA generator [18], which includes a full matrix element computed at NLO. NLO contributions are found to affect the charge asymmetry by 1–2×10^{-2} in the mass range covered by the present analysis, where events are generated with the highest-energy photon in the $20° < \theta^*_\gamma < 160°$ reference range The PHOKHARA results with fully implemented NLO corrections are consistent with the AFKQED results with independent extra photons, with some small discrepancy up to 10^{-2} for masses larger than 4 GeV/c^2. This shows that the small difference between LO and NLO asymmetry originates essentially from kinematic effects due to the extra photon.

The contribution from Z^0 exchange is investigated with the KKMC generator [20], either processed in the QED-only configuration, or including the full $\gamma + Z^0$ exchange diagrams. As in AFKQED, extra photons are generated independently in the initial state and final state (with PHOTOS). Electroweak (EW) effects are found to be at a few 10^{-3} level, averaging over the full mass range.

A significant difference of $(0.81 \pm 0.16) \times 10^{-2}$ is observed between the asymmetry slopes in KKMC and AFKQED, with an asymmetry slope A_0 larger (in absolute value) in AFKQED than in KKMC. The conclusion holds if one considers the forward and backward hemispheres separately. As already observed for AFKQED, the asymmetries expected from KKMC in the two hemispheres are consistent with each other.

Comparison of the asymmetry slope measured in data, after acceptance correction, to the full QED + Z

expectation, as implemented in KKMC, confirms that a significant difference of 2×10^{-2} remains in the 1.5–4 GeV/c^2 mass interval, mostly in the forward hemisphere ($\cos\theta^*_\gamma > 0$).

4. Conclusion on systematic uncertainties

In the large number of tests, both experimental and theoretical, that have been performed, the antisymmetric part (A_0) of the charge asymmetry is found to be remarkably stable. It is immune to all detector effects taken into account in the simulation, unlike the symmetric part (B_0). The simulation properly corrects known effects after data/MC adjustment of separate sources. The experimental absolute systematic uncertainties on A_0 are estimated to be 0.5×10^{-2} from MC reweighting, 0.3×10^{-2} from data/MC efficiency corrections, and 0.7×10^{-2} from acceptance edge effects, which sum up to 0.9×10^{-2}. In view of the observed differences on A_0 using AFKQED, PHOKHARA 9.0 (LO and NLO) and KKMC (with and without EW corrections), we conservatively set a 1.0×10^{-2} systematic uncertainty on the theoretical prediction. Adding experimental and theoretical uncertainties quadratically a total absolute systematic uncertainty of 1.4×10^{-2} is obtained.

Although we have been unable to find a bias producing the observed shape as a function of mass of the difference between the measured A_0 and the QED predictions, all data points are within the estimated systematic uncertainty, except for five out of 14 points near 3 GeV/c^2 that exceed the systematic uncertainty by about 1–2 statistical standard deviations.

VII. RESULTS ON THE CHARGE ASYMMETRY IN THE $e^+e^- \to \pi^+\pi^-\gamma$ PROCESS

The charge asymmetry for $e^+e^- \to \pi^+\pi^-\gamma$ data before and after background subtraction and efficiency corrections is shown in Fig. 21. As for $e^+e^- \to \mu^+\mu^-\gamma$, the background for the $\pi^+\pi^-\gamma$ process is estimated with MC, as explained in Sec. IV E. The overall efficiency is obtained with full simulation of $e^+e^- \to \pi^+\pi^-\gamma$ events, as a function of $\cos\phi^*$ at respective $\pi\pi$ masses, and corrected for data/MC differences in detector response.

The slopes A_0 of charge asymmetry in various $m_{\pi\pi}$ intervals are obtained by fitting the corrected charge asymmetry distributions to $A_0 \cos\phi^*$. The results for the data are shown in Fig. 22 as a function of $m_{\pi\pi}$. In the ρ resonance region, the measured asymmetry is negative, and its magnitude does not exceed $\sim 10^{-2}$. A clear interference pattern is observed at higher mass.

A. Comparison and fit to models

The magnitude of the charge asymmetry, and its variation with mass, measured in the $\pi^+\pi^-\gamma$ data (Fig. 22) is quite different from the prediction of the FSR model 1, which treats the pion as a point-like particle (Sec. III B 1). This model is not considered any further. Instead the *a priori* more realistic quark FSR model 2 (Sec. III B 2), with the modified form of the GDA formula [Eq. (12)], is used to fit the data. The S-wave and D-wave magnitudes ($c_{0,2}$) are left free in the fit, while the mass m_{f_2} and width Γ_{f_2} for the $f_2(1270)$ resonance are fixed to the world averages [29]. Because the measured charge asymmetry loses precision near the $\pi\pi$ production threshold and above 1.4 GeV/c^2, the fit is performed between 0.3 and 1.4 GeV/c^2. The upper limit removes the delicate region around 1.5 GeV/c^2 where the pion form factor has a very pronounced dip leading to a poor knowledge of the ISR amplitude.

A distinctive interference pattern is observed in Fig. 22 at the location of the $f_2(1270)$ resonance. In Eq. (12), assuming the dominance of helicity 0 for the f_2 production, the angular dependence of the interference term in the $\pi\pi$ c.m. is given by the Legendre polynomial $P_2(\cos\theta^*)$, which changes sign at $|\cos\theta^*| = 1/\sqrt{3}$. As a consequence, the charge asymmetry is expected to follow the same pattern in the vicinity of the $f_2(1270)$ resonance.

To check this feature, the charge asymmetries are measured separately in the phase space below and above $|\cos\theta^*| = 1/\sqrt{3}$. The data sample is split according to the additional requirement $|\cos\theta^*| < 1/\sqrt{3}$, or $|\cos\theta^*| > 1/\sqrt{3}$. To enhance the efficiency in the high-$|\cos\theta^*|$ region, the event selection is loosened, by removing the $p > 1\,\mathrm{GeV}/c$ and pion identification requirements on the track with lower momentum. To keep backgrounds at manageable levels, the higher-momentum pion is required to satisfy the tighter identification criteria of a "hard π" [6]. To further reduce the electron contamination, an enhanced $E_{\mathrm{cal}}/p < 0.6$ selection is applied to the high-momentum track, and the ionization energy loss in the DCH of the low-momentum track is required to be below the average electron loss ($\mathrm{d}E/\mathrm{d}x_{\mathrm{DCH}} < 650$). The corresponding efficiencies are obtained separately from the full simulation of $e^+e^- \to \pi^+\pi^-\gamma$ events in the low- and high-$|\cos\theta^*|$ regions. While the effective $|\cos\theta^*|$ range is limited to $|\cos\theta^*| < 0.8$ with the standard event selection, the specific selection applied in the high-$|\cos\theta^*|$ region allows us to extend the asymmetry measurement up to $|\cos\theta^*| \sim 0.95$. Backgrounds are estimated accordingly using the full simulation of relevant processes. After background subtraction and overall acceptance correction, the charge asymmetries obtained for $|\cos\theta^*|$ below and above $1/\sqrt{3}$ are shown in Fig. 23.

Since a large fraction of the events in the standard analysis are in the low-$|\cos\theta^*|$ region, the charge asymmetry measured with $|\cos\theta^*| < 1/\sqrt{3}$ is quite close to the one obtained using the full sample (Fig. 22). Although limited by statistics, the charge asymmetry measured in the high-$|\cos\theta^*|$ region presents the opposite sign oscillation around the $f_2(1270)$ mass, which is the expected pattern.

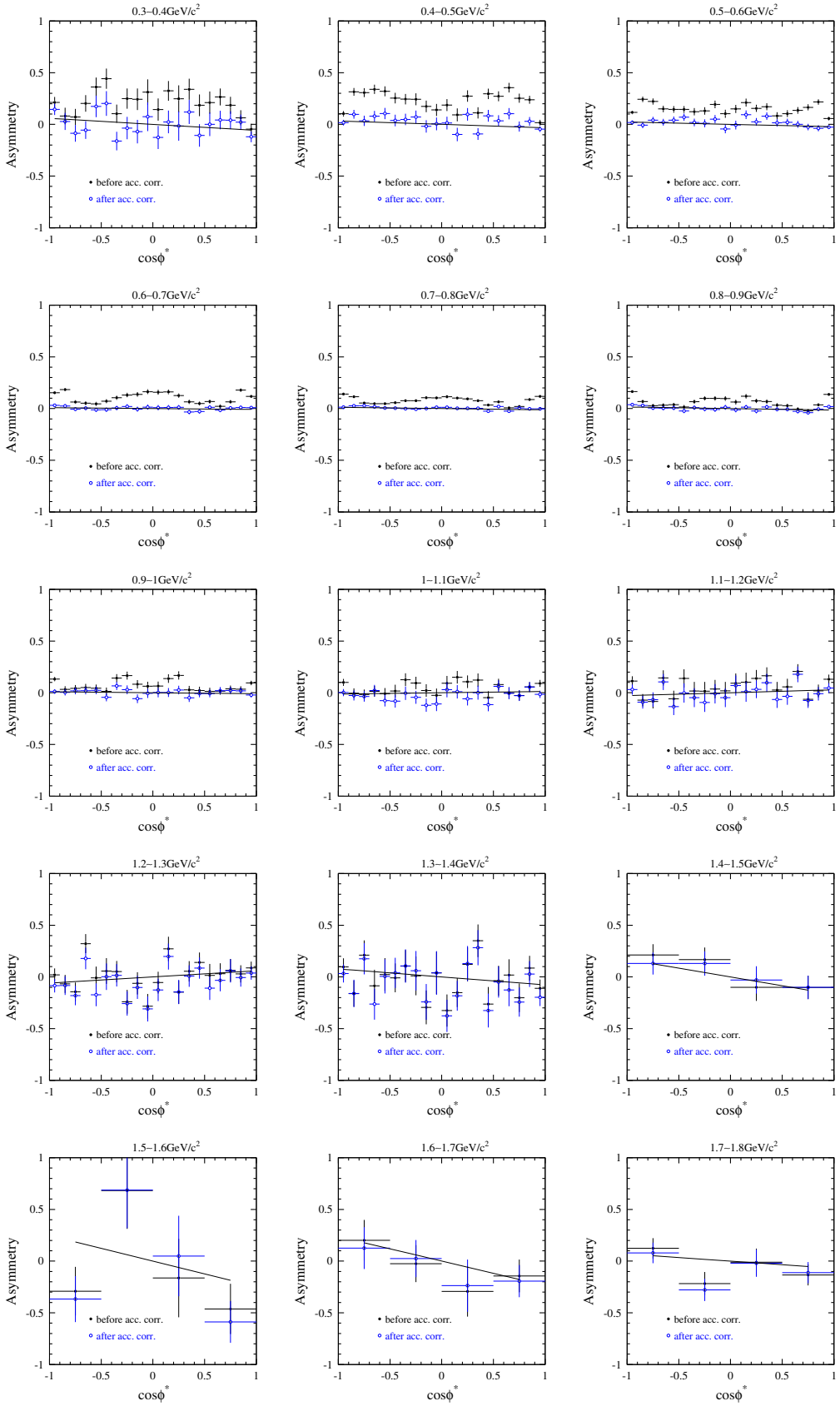

FIG. 21 (color online). Charge asymmetry for $e^+e^- \to \pi^+\pi^-\gamma$ data before (•) and after (○) efficiency corrections, in 0.1 GeV/c^2 mass intervals from 0.3 to 1.8 GeV/c^2. The line shows the result of the fit to $A_0 \cos\phi^*$.

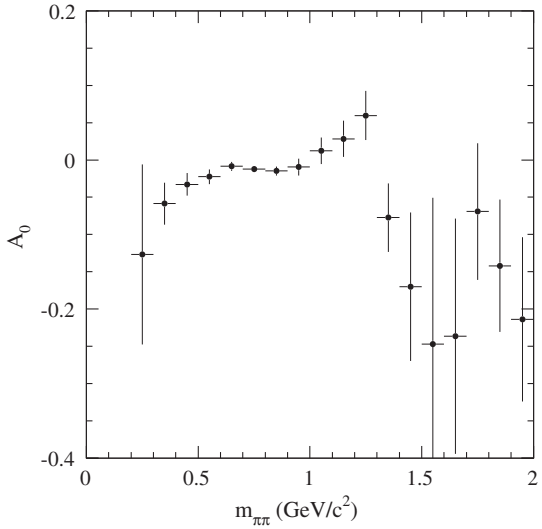

FIG. 22. The fitted slope A_0 of the charge asymmetry for $e^+e^- \to \pi^+\pi^-\gamma$ at $\sqrt{s} = 10.58\,\mathrm{GeV}$, corrected for efficiency within the $20° < \theta^*_\gamma < 160°$ acceptance in the e^+e^- c.m.

The change of sign between $|\cos\theta^*| < 1/\sqrt{3}$ and $|\cos\theta^*| > 1/\sqrt{3}$, and the opposite variation across the resonance provide a solid validation that the observed charge asymmetry around the $f_2(1270)$ resonance is indeed due to the interference between the two amplitudes for $e^+e^- \to \gamma_{\mathrm{ISR}}\pi^+\pi^-$ and $e^+e^- \to \gamma_{\mathrm{FSR}} f_2(1270)(\pi^+\pi^-)$, with f_2 in the helicity-0 state. In the mass range below $1\,\mathrm{GeV}/c^2$, the asymmetry keeps the same (negative) sign in the two $|\cos\theta^*|$ regions, as expected for the interference with a scalar amplitude flat in $|\cos\theta^*|$.

The two independent data samples, with $|\cos\theta^*|$ below and above $1/\sqrt{3}$, are fitted separately to the model, and the fitted c_0 and c_2 amplitudes are obtained in both cases. Since

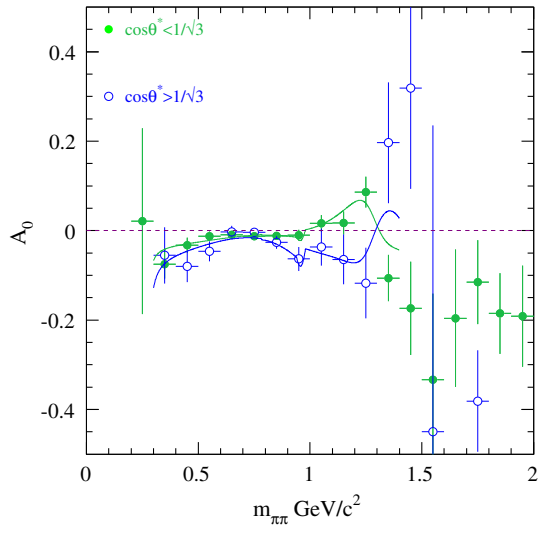

FIG. 23 (color online). The charge asymmetries measured with $|\cos\theta^*|$ below and above $1/\sqrt{3}$. The curves represent the fit results (see text).

the pure ISR AFKQED MC used to compute the efficiencies is not expected to properly correct for unmeasured regions of $|\cos\theta^*|$, the fit of the data above $1/\sqrt{3}$ is performed in the effective range of non-null efficiency where asymmetries are measurable.

The model describes the data well, and the two sets of fitted values of c_0 and c_2 are consistent in sign and magnitude and can be averaged, yielding $c_0 = -1.27 \pm 0.20$ and $c_2 = 5.4 \pm 1.6$.

B. Monte Carlo reweighting and final results

Since a significant asymmetry is observed in the data in contrast with AFKQED, which does not include LO FSR in the pion channel, the overall efficiencies $\epsilon_\pm$ computed with MC and used to measure the asymmetry in data are biased through the cross effect between the acceptance and the physical asymmetry (Sec. V A 1). This situation calls for an iterative procedure to introduce the observed interference effect into the MC.

To implement this procedure, new MC samples of reweighted events are produced, in which the weights are computed event by event as the full cross section value including LO FSR divided by the ISR-only cross section, for the values of $m_{\pi\pi}$, $\cos\theta^*_\gamma$, $\cos\theta^*$ and $\cos\phi^*$ for the event. The differential cross sections are given by the model used to fit the data [Eqs. (8)–(10)]. The FSR model is made quantitative by using the fitted values for $c_{0,2}$. The studies have been performed separately for the regions below and above $1/\sqrt{3}$.

The fitted values of c_0 and c_2 are stable after two iterations. A third iteration is performed in order to check the stability of the results. The difference between the last two iterations is taken as a systematic uncertainty.

The final A_0 values are given in Fig. 24, together with the FSR model prediction using the fitted $c_{0,2}$ values determined by the iterative process. The extrapolation of the model beyond the fit region 0.3–1.4 GeV/c^2 is shown (light-blue band). Although the statistical uncertainty of the data is large, there is evidence that the model becomes inadequate above $1.8\,\mathrm{GeV}/c^2$. This is not surprising since a constant S-wave amplitude and the f_2 resonance are likely to be insufficient to describe this region, where many high-mass resonances contribute to the $\pi^+\pi^-$ final state. However, based on the change of asymmetry at the 10^{-3} level induced at lower mass, the effect of inadequate reweighting in the last few mass bins is expected to be much smaller than the statistical uncertainty.

Since the two independent sets of parameters agree within their uncertainties, they can be combined and the weighted average of the fitted values represents the best information which can be obtained from this interference analysis (Table II). An alternative is to fit the overall sample obtained with the standard selection, using efficiencies calculated with the reweighted MC. In this case, as

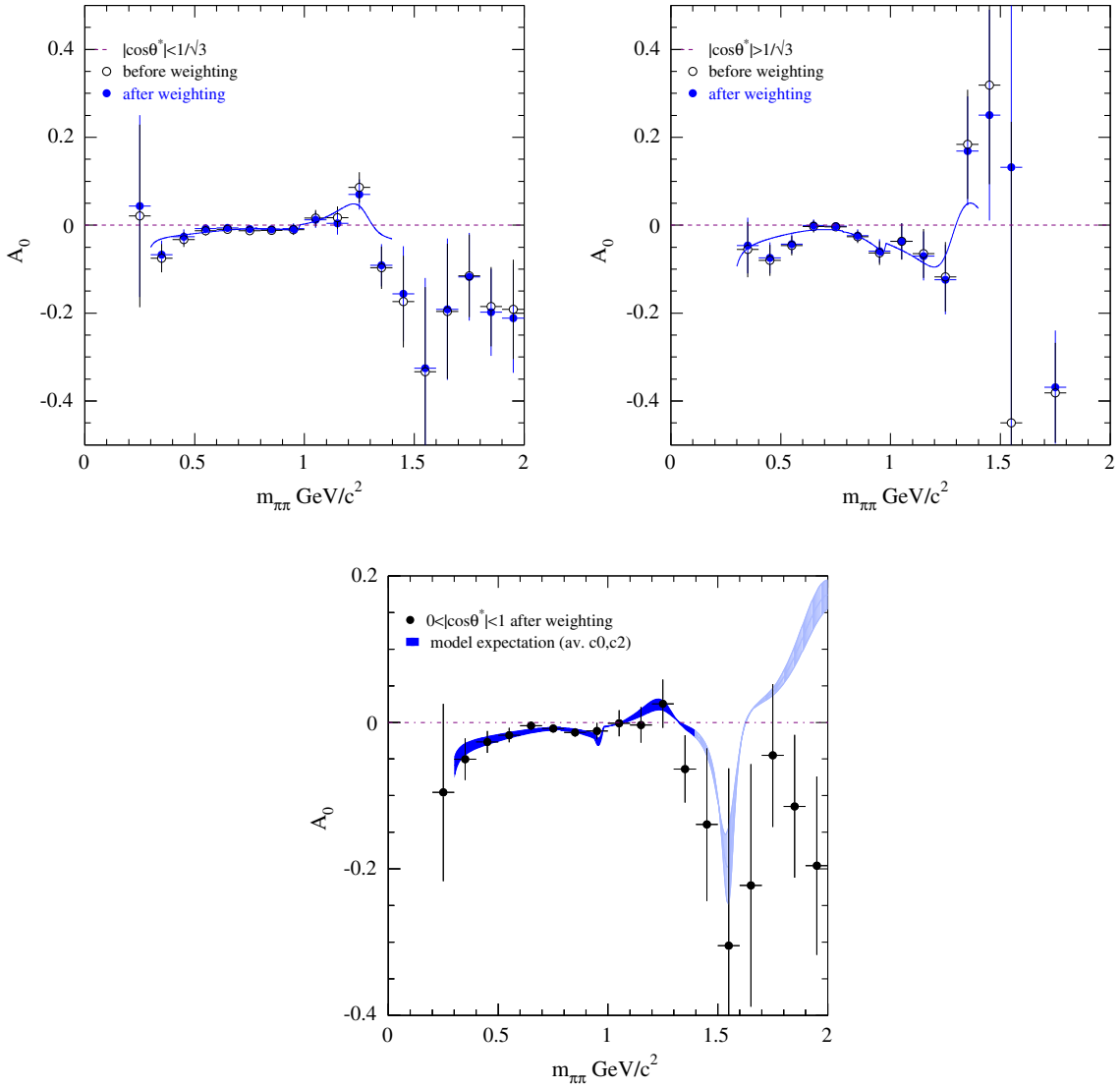

FIG. 24 (color online). The charge asymmetry slopes for $e^+e^- \to \pi^+\pi^-\gamma$ using MC samples with and without reweighting, and fit to the model after reweighting (see text) for (top left) $|\cos\theta^*| < 1/\sqrt{3}$, (top right) $|\cos\theta^*| > 1/\sqrt{3}$, and (bottom) for the full $|\cos\theta^*|$ range; the blue band represents the model-2 prediction using the average $c_{0,2}$ values after reweighting. The light-blue part corresponds to the extrapolation of the model beyond the fitted range.

the data spans over the sign change at $|\cos\theta^*| = 1/\sqrt{3}$, the measured asymmetry is much reduced. Therefore the combined result from the two complementary ranges is more sensitive, and moreover provides a clear confirmation of the helicity-0 $f_2(1270)$ contribution.

C. Systematic uncertainties

The difference ΔA_0 between the results with and without background subtraction is found to be less than 10^{-3}, except near threshold (1×10^{-2}) and above $1.1\,\mathrm{GeV}/c^2$ (1×10^{-2} at $1.25\,\mathrm{GeV}/c^2$). Except in the dip region at

TABLE II. The parameters obtained from the fit of the charge asymmetry for $e^+e^- \to \pi^+\pi^-\gamma$ at $\sqrt{s} = 10.58\,\mathrm{GeV}$ after three iterations, with $20° < \theta^*_\gamma < 160°$ in the e^+e^- c.m., in the $|\cos\theta^*|$ below and above $1/\sqrt{3}$ regions, and the weighted average, where the errors are statistical. The results of the direct fit over the full range are given in the last column.

parameter	$\lvert\cos\theta^*\rvert < 1/\sqrt{3}$	$\lvert\cos\theta^*\rvert > 1/\sqrt{3}$	average	all $\lvert\cos\theta^*\rvert$
c_0	-0.84 ± 0.24	-1.13 ± 0.35	-0.93 ± 0.20	-0.87 ± 0.20
c_2	3.82 ± 1.81	6.33 ± 3.03	4.48 ± 1.56	3.41 ± 4.25

$1.55\,\mathrm{GeV}/c^2$ where the ISR cross section has a sharp minimum and statistical uncertainties are very large, the background level has been checked [6] with a precision of 20% in the worst cases. The systematic uncertainty due to background subtraction is consequently estimated to be less than 2×10^{-4} from 0.4 to $1.1\,\mathrm{GeV}/c^2$, increasing above (2×10^{-3} at $1.25\,\mathrm{GeV}/c^2$).

As observed for $e^+e^-\to\mu^+\mu^-\gamma$, the selection requirements for trigger, tracking, and π-ID have charge-asymmetric efficiencies for the $e^+e^-\to\pi^+\pi^-\gamma$ process. The corrections for the difference between data and MC on the efficiencies are included in the overall acceptance. The difference between the charge asymmetry results with and without the data-MC corrections is smaller than 10^{-3} except in the dip region (0.5×10^{-2}). Since the corrections are determined with data with a precision of 10%, the resulting systematic uncertainty is negligible.

As done for $\mu^+\mu^-\gamma$, the asymmetry $A(\cos\phi^*)$ in $\pi^+\pi^-\gamma$ is alternatively fitted to $A_0\cos\phi^*+B_0$ since a bias on A_0 and B_0 values inconsistent with zero might disclose an incorrect efficiency determination, or an incorrect background subtraction. As shown in Fig. 25, the fitted slopes A_0 deviate from the final values by less than 10^{-3}, except in the background-dominated dip region of the cross section ($m_{\pi\pi}\simeq1.5\,\mathrm{GeV}/c^2$), where the deviation ΔA_0 reaches 3×10^{-2}. In the $m_{\pi\pi}$ region where the fit of the theoretical model is performed (0.3–$1.4\,\mathrm{GeV}/c^2$), the slope A_0 does not change by more than 5×10^{-4}, except in the last (1.3–$1.4\,\mathrm{GeV}/c^2$) bin, where the deviation is 2×10^{-3}. This is consistent with the estimated background contribution to the systematic error. The fitted B_0 values are within 2.5σ from zero over the full mass range. The average B_0 for $m_{\pi\pi}<1\,\mathrm{GeV}/c^2$ is $(0.41\pm0.16)\times10^{-2}$.

Different interaction rates in the detector material for positive and negative pions induce a charge asymmetry. Although such an effect is included in the simulation of the detector response based on GEANT4, its description and the corresponding track loss are known to be somewhat imperfect. Independent studies have shown that data/MC discrepancies occur at the 10% level for both π^+ and π^-, in opposite directions. A residual charge asymmetry is thus expected after applying the MC corrections. The effect of imperfect simulation of nuclear interactions is investigated using the large sample of $\pi^+\pi^-\gamma$ events produced by AFKQED at the generator level. A weight is assigned to each track according to its momentum and its path length through detector material as a function of the polar angle, using a $\pm10\%$ relative change in the respective π^+ and π^- interaction rates. The charge asymmetry obtained after the interaction reweighting is subjected to the two-parameter linear fit in the integrated mass range from 0.4 to $1.2\,\mathrm{GeV}/c^2$. The slope A_0 changes by only $\Delta A_0=(-0.006\pm0.024)\times10^{-2}$, which confirms the robustness of the A_0 observable. The charge asymmetry itself is however modified as the fitted B_0 value is found to be displaced significantly, $\Delta B_0=(0.240\pm0.016)\times10^{-2}$, in good agreement with the observed B_0 value in data in the same mass range. Imperfect simulation of nuclear interactions thus provides a plausible explanation of the small B_0 values found in the analysis, while leaving the A_0 measurement unaffected.

Summing up all sources, including the estimated cross-effect between acceptance and physical asymmetry, the absolute systematic uncertainty on A_0 is estimated to be less than 0.17% in the $f_2(1270)$ region and less than 0.1% elsewhere.

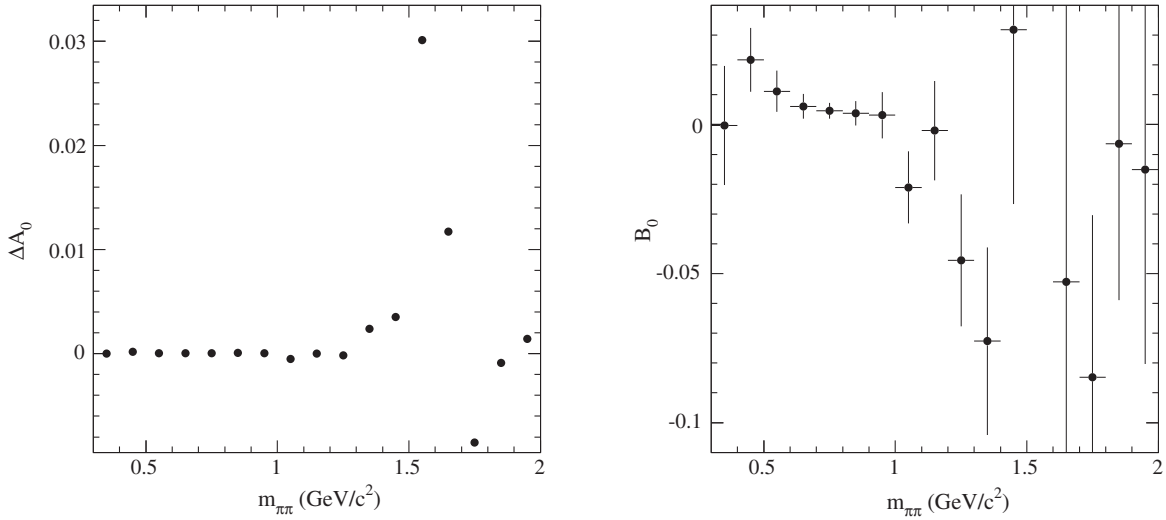

FIG. 25. The change of slope ΔA_0 (left) and constant term B_0 (right) in the fit of charge asymmetry to $A_0\cos\phi^*+B_0$, as a function of $\pi\pi$ mass for $e^+e^-\to\pi^+\pi^-\gamma$.

D. Searching for an $f_2(1270)$ signal in the $\pi^+\pi^-\gamma$ cross section

Given the sizable amplitude c_2 of the D-wave contribution to the ISR-FSR interference obtained from the charge asymmetry measurement, direct evidence of $f_2(1270)$ production is searched for in the cross-section measurement. While the latter is overwhelmingly dominated by the ISR production of the ρ resonance, the rapid fall off of the pion form factor in the vicinity of the $f_2(1270)$, and the distinct angular distribution $P_2(\cos\theta^*)$ of the D-wave in the $\pi\pi$ system, are assets used in the direct search.

Since the $P_2(\cos\theta^*)$ distribution exhibits a peak at $|\cos\theta^*|$ near unity, in contrast with the $\sin^2\theta^*$ dependence of the ISR cross section, the search is performed in the very high range $|\cos\theta^*| > 0.85$. Because the standard event selection depopulates that region completely, due to the momenta of both tracks being required to be larger than $1\,\mathrm{GeV}/c$, the direct search uses the specific selection designed for the charge asymmetry measurement in the high-$|\cos\theta^*|$ region (Sec. VII A), with an even tighter $\mathrm{d}E/\mathrm{d}x_{\mathrm{DCH}} < 550$ requirement.

The $\pi\pi$ mass spectrum of the reconstructed events in this specific analysis is displayed in Fig. 26 with the largest expected background from $\mu\mu\gamma$ events to be subtracted. The resulting spectrum is dominated by the ISR production, which is also subtracted. The remaining spectrum shown in Fig. 27 does not present any significant excess at the $f_2(1270)$ mass or elsewhere, except for a slow rise above $2\,\mathrm{GeV}/c^2$ (not shown) that originates from a residual $ee\gamma$ background. The mass spectrum is fitted between 0.95 and $1.95\,\mathrm{GeV}/c^2$ to a constant and a Breit-Wigner line shape

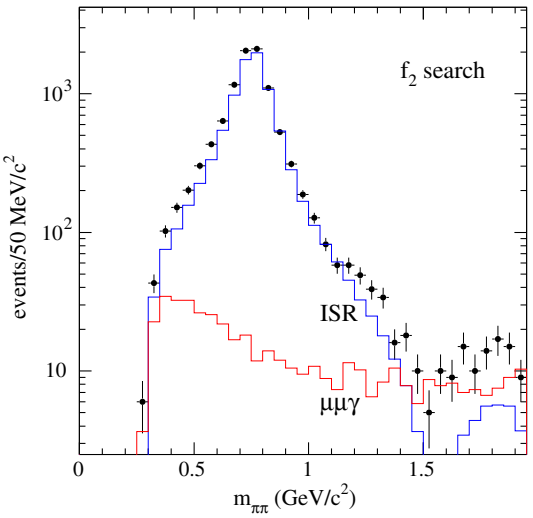

FIG. 26 (color online). The $\pi\pi$ mass spectrum for $|\cos\theta^*| > 0.85$ for the analysis extended to low momentum (points), the expected background from misidentified $\mu\mu\gamma$ events (red histogram), and the predicted ISR spectrum from the standard cross-section analysis (blue histogram).

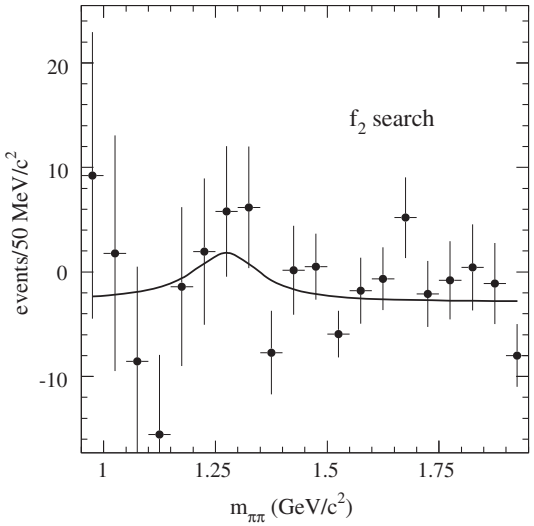

FIG. 27. The $\pi\pi$ mass spectrum for $|\cos\theta^*| > 0.85$ for the analysis extended to low momentum (points) after subtraction of the $\mu\mu\gamma$ background and the ISR contribution. The curve is the result of a fit to a constant term and a simple Breit-Wigner shape for the f_2 resonance.

with the world average $f_2(1270)$ mass and width [29] and a free-floating amplitude. The fitted number of f_2 events in the mass interval at the peak is found to be 4.7 ± 4.2, to be compared to 26.7 ± 1.1 ISR events in the same interval. After correction for the loss of efficiency near $|\cos\theta^*| = 1$ obtained from MC for ISR and f_2 candidates, the $f_2(1270)$ fraction $|f_2|^2/(|\mathrm{ISR}|^2 + |f_2|^2)$ in the f_2-enhanced range $0.8 < |\cos\theta^*| < 1$ is measured to be 0.22 ± 0.15. This corresponds to a $|c_2|$ value equal to 4.6 ± 2.2.

The three independent determinations of $|c_2|$ [the interference fits in two $\cos\theta^*$ regions and the direct $f_2(1270)$ search in the cross section] yield consistent results. Since a positive sign is clearly indicated by the interference analysis, the value from the direct search is also taken to be positive. The three independent values can be combined with the result $c_2 = 4.5 \pm 1.3$, establishing LO FSR production of the $f_2(1270)$ resonance at the 3.6σ level. The corresponding production cross section is (37^{+24}_{-18}) fb. The results are displayed in Fig. 28. The size of c_2 is about a factor of 2 larger than the value predicted by Chernyak [30] with a QCD model giving $|c_2^{\mathrm{th}}| = 2.2$. However the difference only amounts to 1.8σ, not including the unknown theoretical uncertainty. The sign is not provided in Chernyak's prediction.

E. Consequences for the cross-section measurement by *BABAR* for $e^+e^- \to \pi^+\pi^-$ and the contribution to the anomalous magnetic moment of the muon

In the measurement of the $e^+e^- \to \pi^+\pi^-$ cross section by the *BABAR* Collaboration [6] using the ISR method, the lowest-order FSR contribution was argued to be negligible, based on theoretical estimates. The primary result of the

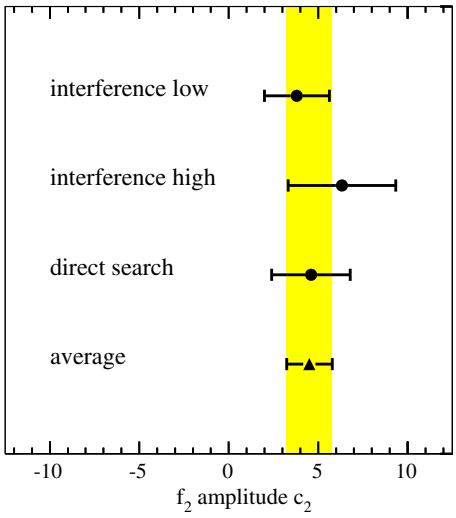

FIG. 28 (color online). The results obtained for the $f_2(1270)$ amplitude c_2 in the process $e^+e^- \to \pi^+\pi^-\gamma$ from the interference analysis and the direct $f_2(1270)$ search in the cross section. The labels "low" and "high" refer to the determination in the two angular ranges $|\cos\theta^*| < 1/\sqrt{3}$ and $1/\sqrt{3} < |\cos\theta^*|$. For the direct search the positive solution is chosen. The combined value for the three independent analyses is given by the vertical band.

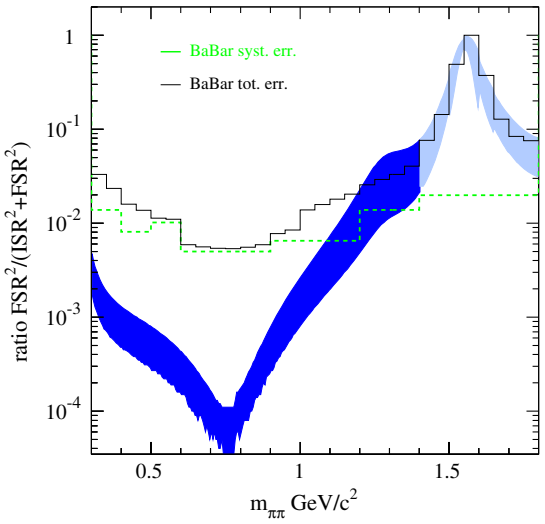

FIG. 29 (color online). The FSR fraction in the *BABAR* measurement [6] of the $\pi\pi\gamma$ cross section, defined as the ratio $\frac{|\mathcal{M}_{\rm FSR}|^2}{|\mathcal{M}_{\rm ISR}|^2+|\mathcal{M}_{\rm FSR}|^2}$ obtained in this analysis using FSR model 2 with $c_{0,2}$ parameters fitted to data (blue band). The light-blue part corresponds to the extrapolation of the model beyond the fitted range. The FSR fraction is compared to the systematic error of the *BABAR* cross-section measurement (green dashed histogram) and its total error (black histogram).

present interference analysis is to determine the actual size of the $|\mathcal{M}_{\rm FSR}|^2$ cross section, misinterpreted as ISR, and its contribution to the total cross section $(|\mathcal{M}_{\rm ISR}|^2 + |\mathcal{M}_{\rm FSR}|^2)$.

Using the FSR model 2, which describes well the measured charge asymmetry in the $[0.3\text{–}1.4]\,\mathrm{GeV}/c^2$ range, the FSR cross section calculated through Eq. (9) with the fitted $c_{0,2}$ parameters, is extrapolated to higher masses. The resulting FSR fraction in the *BABAR* cross section is given in Fig. 29 as a function of $m_{\pi\pi}$. As expected the FSR fraction is negligible in the ρ region, but increases significantly above $1\,\mathrm{GeV}/c^2$ due to the $f_2(1270)$ contribution and the rapid falloff of the pion form factor. In fact the FSR "background" exceeds the estimated systematic uncertainty quoted in Ref. [6] (green histogram in Fig. 29) for mass above $1.2\,\mathrm{GeV}/c^2$, while remaining close to the total uncertainty (black histogram). The FSR contribution is found to be dominant around $1.5\,\mathrm{GeV}/c^2$, in the region where the ISR cross section displays a deep dip and is consistent with zero within the large errors.

The contribution to the muon magnetic anomaly, $a_\mu = (g_\mu - 2)/2$, from hadronic vacuum polarization involves a dispersion integral over the cross section $e^+e^- \to$ hadrons weighted by a known kernel (Ref. [31] and references therein). The integral is dominated by the $\pi^+\pi^-$ channel and its most precise determination to date is from *BABAR* using the ISR method [6] with the value $a_\mu^{\pi\pi(\gamma),\mathrm{LO}} = (514.09 \pm 2.22_{\rm stat} \pm 3.11_{\rm syst}) \times 10^{-10}$ when integrating from threshold to 1.8 GeV. This value is derived under the assumption that the cross section for $e^+e^- \to \pi^+\pi^-\gamma(\gamma)$ has a negligible contribution from LO FSR.

The present measurement of the charge asymmetry allows one to validate this assumption in a quantitative way. Using the FSR fraction shown in Fig. 29, the contribution to a_μ from the LO FSR falsely attributed to the ISR cross section is found to be, in the same energy range up to 1.8 GeV

$$\Delta a_\mu^{\pi\pi}(\mathrm{FSR}) = (0.26 \pm 0.12) \times 10^{-10}. \qquad (17)$$

This reduces the value of $a_\mu^{\pi\pi}$ by $(5.1 \pm 2.3) \times 10^{-4}$ relative to the *BABAR* determination. The correction is small compared to the total *BABAR* relative uncertainty of 7.4×10^{-3}, which justifies its earlier neglect.

VIII. CONCLUSIONS

The radiative process $e^+e^- \to X\gamma$, where $X = \mu^+\mu^-$ and $\pi^+\pi^-$ are considered in this analysis, involves contributions from both LO ISR and FSR. Because charge parities of the final-state pair are opposite for ISR and FSR, the interference between ISR and FSR changes sign with the charge interchange of the two muons (pions). As a consequence, investigation of the charge asymmetry of the process gives a way to study the interference between ISR and FSR, which is sensitive to the relative contribution of LO FSR.

From QED for $\mu^+\mu^-\gamma$, and from FSR models for $\pi^+\pi^-\gamma$, we find that the charge asymmetry A has a strong dependence on the angle ϕ^* between the $\mu^-\mu^-$ $(\pi^+\pi^-)$ plane and the $e^+e^-\gamma$ plane in the e^+e^- c.m. system, which can be simply represented by a linear function

$A = A_0 \cos\phi^*$. The slope A_0 quantifies the magnitude of the interference between ISR and FSR.

The acceptance effects on the measured charge asymmetry are studied with the full simulation of $e^+e^- \to \mu^+\mu^-\gamma$ and $e^+e^- \to \pi^+\pi^-\gamma$ events. We find that the detector and event selection, including trigger, tracking, PID, and kinematic fitting, induce nonlinear patterns on the $\cos\phi^*$ dependence of the charge asymmetry, but have a small impact on the determined slope A_0. Kinematic acceptance—namely the angular acceptance, and energy or momentum requirements on the final-state particles—changes the slope of the observed charge asymmetry significantly, although the kinematic requirements are charge symmetric. This is due to a cross effect between acceptance and true interference that produces a bias in the measured asymmetry if the physical asymmetry differs between data and MC. This bias is corrected through an iterative procedure in the $\pi^+\pi^-\gamma$ analysis, as in that case the charge asymmetry is null in the generator.

After background subtraction and correction for the overall acceptance, which are obtained from the full simulation with corrections for data/MC differences, we measured the slope A_0 of the charge asymmetry as a function of $m_{\mu\mu}$ ($m_{\pi\pi}$). The QED test, namely the comparison between the charge asymmetry measured in the $\mu^+\mu^-\gamma$ data and predicted by the simulation, in which the LO ISR-FSR interference is implemented, shows an overall good consistency. However, some absolute deviation amounting to $\Delta A_0 = A_0^{\rm data} - A_0^{\rm MC} \simeq 0.03$ in the $3\,{\rm GeV}/c^2$ region is observed and cannot be fully explained by known systematic effects, either in the data or in the MC generators, which are estimated to be less than 0.014.

The measured slope A_0 of charge asymmetry in the $e^+e^- \to \pi^+\pi^-\gamma$ data is about -1% and flat around the ρ mass. Outside of the ρ peak, the data exhibits the pattern expected from the interference between $e^+e^- \to \gamma_{\rm ISR}\pi^+\pi^-$ and $e^+e^- \to \gamma_{\rm FSR} f_2(1270)(\pi^+\pi^-)$. The data shows a good consistency with the predictions of a model of FSR from quarks with contributions of a scalar widespread mass distribution and the $f_2(1270)$ tensor resonance. In the ρ region the results are not consistent with a model based on FSR from point-like pions (scalar QED), in contrast with the observations at low energies [4].

These results are first measurements of the charge asymmetry in the $e^+e^- \to \mu^+\mu^-\gamma$ process, and for $e^+e^- \to \pi^+\pi^-\gamma$ at high energy ($\sqrt{s} \sim 10.58\,{\rm GeV}$). The FSR contribution to $e^+e^- \to \pi^+\pi^-\gamma$ derived from this analysis is small and this confirms that it is negligible in the measurement of the cross section obtained by *BABAR* assuming pure ISR [6]. Accordingly this FSR bias translates into a correction to the muon magnetic anomaly of only (0.51 ± 0.23) per mille of the $\pi\pi$ hadronic vacuum polarization determined from *BABAR* data, small compared to the total quoted uncertainty of 7.4 per mille.

ACKNOWLEDGMENTS

We gratefully acknowledge useful discussions on theoretical issues with H. Czyż, Zhun Lu and B. Pire, and clarifications by A. B. Arbuzov, S. J. Brodsky, R. Gastmans, and R. Kleiss. We thank Henryk Czyż for providing tests with PHOKHARA-V9. We are grateful for the extraordinary contributions of our PEP-II colleagues in achieving the excellent luminosity and machine conditions that have made this work possible. The success of this project also relies critically on the expertise and dedication of the computing organizations that support *BABAR*. The collaborating institutions wish to thank SLAC for its support and the kind hospitality extended to them. This work is supported by the US Department of Energy and National Science Foundation, the Natural Sciences and Engineering Research Council (Canada), the Commissariat à l'Energie Atomique and Institut National de Physique Nucléaire et de Physique des Particules (France), the Bundesministerium für Bildung und Forschung and Deutsche Forschungsgemeinschaft (Germany), the Istituto Nazionale di Fisica Nucleare (Italy), the Foundation for Fundamental Research on Matter (The Netherlands), the Research Council of Norway, the Ministry of Education and Science of the Russian Federation, Ministerio de Economía y Competitividad (Spain), the Science and Technology Facilities Council (United Kingdom), and the Binational Science Foundation (U.S.-Israel). Individuals have received support from the Marie-Curie IEF program (European Union) and the A. P. Sloan Foundation (USA).

[1] V. N. Baier and V. S. Fadin, Phys. Lett. B **27**, 223 (1968).
[2] A. B. Arbuzov, E. A. Kuraev, N. P. Merenkov, and L. Trentadue, J. High Energy Phys. 12 (1998) 009.
[3] S. Binner, J. H. Kühn, and K. Melnikov, Phys. Lett. B **459**, 279 (1999).
[4] M. Benayoun, S. I. Eidelman, V. N. Ivanchenko, and Z. K. Silagadze, Mod. Phys. Lett. A **14**, 2605 (1999).
[5] A. Bevan *et al.* (*BABAR* and Belle Collaborations), Chap. 21, Eur. Phys. J. C **74**, 3026 (2014).
[6] B. Aubert *et al.* (*BABAR* Collaboration), Phys. Rev. Lett. **103**, 231801 (2009); J. P. Lees *et al.* (*BABAR* Collaboration), Phys. Rev. D **86**, 032013 (2012).
[7] S. E. Muller *et al.* (KLOE Collaboration), Chin. Phys. C **34**, 686 (2010).

[8] H. Czyż, A. Grzelińska, and J. H. Kühn, Phys. Lett. B **611**, 116 (2005).
[9] R. Gastmans and T. T. Wu, *The Ubiquitous Photon* (Clarendon, Oxford, 1990).
[10] F. A. Berends and R. Kleiss, Nucl. Phys. **B177**, 237 (1981).
[11] A. B. Arbuzov, E. A. Kuraev, G. V. Fedotovich, N. P. Merenkov, V. D. Rushai, and L. Trentadue, J. High Energy Phys. 10 (1997) 001.
[12] T. K. Pedlar *et al.* (CLEO Collaboration), Phys. Rev. Lett. **95**, 261803 (2005).
[13] H. Czyż, J. H. Kühn, E. Nowak, and G. Rodrigo, Eur. Phys. J. C **35**, 527 (2004); **39**, 411 (2005).
[14] Z. Lu and I. Schmidt, Phys. Rev. D **73**, 094021 (2006); **75**, 099902(E) (2007).
[15] A. B. Arbuzov, E. A. Kuraev, V. A. Astakhov, G. V. Fedotovich, A. V. Fedorov, and N. P. Merenkov, J. High Energy Phys. 10 (1997) 006.
[16] M. Diehl, T. Gousset, and B. Pire, Phys. Rev. D **62**, 073014 (2000).
[17] B. Hyams *et al.*, Nucl. Phys. **B64**, 134 (1973).
[18] F. Campanario, H. Czyż, J. Gluza, M. Gunia, T. Riemann, G. Rodrigo, and V. Yundin J. High Energy Phys. 02 (2014) 114.
[19] R. W. Brown and K. O. Mikaelian, Lett. Nuovo Cimento **10**, 305 (1974).
[20] S. Jadach, B. F. L. Ward, and Z. Wąs, Comput. Phys. Commun. **130**, 260 (2000).
[21] J. P. Lees *et al.* (*BABAR* Collaboration), Nucl. Instrum. Methods Phys. Res., Sect. A **726**, 203 (2013).
[22] B. Aubert *et al.* (*BABAR* Collaboration), Nucl. Instrum. Methods Phys. Res., Sect. A **479**, 1 (2002); **729**, 615 (2013).
[23] H. Czyż and J. H. Kühn, Eur. Phys. J. C **18**, 497 (2001).
[24] M. Caffo, H. Czyż, and E. Remiddi, Nuovo Cimento Soc. Ital. Fis. **110A**, 515 (1997).
[25] E. Barberio, B. van Eijk, and Z. Wąs, Comput. Phys. Commun. **66**, 115 (1991).
[26] T. Sjöstrand, Comput. Phys. Commun. **82**, 74 (1994).
[27] S. Jadach and Z. Wąs, Comput. Phys. Commun. **85**, 453 (1995).
[28] H. Czyz (private communication).
[29] J. Beringer *et al.* (Particle Data Group), Phys. Rev. D **86**, 010001 (2012).
[30] V. Chernyak (private communication).
[31] M. Davier, S. Eidelman, A. Höcker, and Z. Zhang, Eur. Phys. J. C **27**, 497 (2003).